

ANALYSIS OF PREFORMED PLASMA CONDITION OF Ni-LIKE Mo X-RAY
LASER MEDIA

A THESIS SUBMITTED TO
THE GRADUATE SCHOOL OF NATURAL AND APPLIED SCIENCES
OF
THE MIDDLE EAST TECHNICAL UNIVERSITY

BY

SEVİNCE

IN PARTIAL FULFILLMENT OF THE REQUIREMENTS
FOR
THE DEGREE OF MASTER OF SCIENCE
IN
PHYSICS

SEPTEMBER 2006

Approval of the Graduate School of Natural and Applied Sciences.

Prof. Dr. Canan Özgen
Director

I certify that this thesis satisfies all the requirements as a thesis for the degree of Master of Science.

Prof. Dr. Sinan Bilikmen
Head of Department

This is to certify that we have read this thesis and that in our opinion it is fully adequate, in scope and quality, as a thesis for degree of Master of Science.

Prof. Dr. Sinan Bilikmen
Supervisor

Examining Committee Members

Prof. Dr. Arif Demir (KOU, PHYS) _____

Prof. Dr. Sinan Bilikmen (METU, PHYS) _____

Prof. Dr. Gülay Öke (METU, PHYS) _____

Assist. Prof. İsmail Rafatov (METU, PHYS) _____

Dr. Burak Yedierler (METU, PHYS) _____

I hereby declare that all information in this document has been obtained and presented in accordance with academic rules and ethical conduct. I also declare that, as required by these rules and conduct, I have fully cited and referenced all material and results that are not original to this work.

Name, Last name: Sevi İnce

Signature :

ABSTRACT

ANALYSIS OF PREFORMED PLASMA CONDITION OF Ni-LIKE Mo X-RAY LASER MEDIA

İNCE, SEVİ

M.S., Department of Physics

Supervisor : Prof. Dr. Sinan Bilikmen

September 2006, 64 pages

The aim of this work is to produce X-ray laser source from a plasma produced by focusing a pulsed laser beam on a solid target. Preformed Molybdenum plasma is created by using Nd:YAG laser pulses with a pulse duration 6 ns and pulse intensity 5.09×10^{11} W/cm². Detailed simulations of Ni-like Mo X-ray laser media are undertaken using the EHYBRID code which is a hydrodynamic code. X-ray resonance lines between 25 Å and 40 Å emitted from the molybdenum plasma have been obtained and analysed. EHYBRID code also gives an information about the electron temperature, electron density, efficient ionization degree and plasma expansion distance of the Ni-like Mo X-ray laser media. An experimental set-up to produce preformed Mo plasma for x-ray laser has been designed for a future work.

Keywords: Ni-like Mo X-ray laser media, EHYBRID code, Plasma, Resonance lines

ÖZ

Ni-BENZERİ Mo X-RAY LAZER ÖNCÜPLAZMA ORTAMININ DURUM ANALİZİ

İNCE, SEVİ

Yüksek Lisans, Fizik Bölümü

Tez Yöneticisi : Prof. Dr. Sinan Bilikmen

Eylül 2006, 64 sayfa

Bu çalışmanın amacı, katı hedefe atımlı lazer ışını odaklayarak X-ray lazer oluşumunu sağlayan plazma ortamı üretmek. Atım uzunluğu 6 ns ve atım şiddeti 5.09×10^{11} W/cm² olan Nd:YAG lazer öncü Molybdenum plazma oluşturmak için kullanıldı. Ni-benzeri Mo X-ray lazer ortamının detaylı simülasyonu hidrodinamik kod olan EHYBRID kullanılarak yapıldı. 25 Å ve 40 Å arasında Mo plazmadan yayılan X-ray rezonans çizgilerinin simülasyonu yapıldı. EHYBRID kod aynı zamanda Ni-benzeri Mo X-ray lazer ortamının elektron sıcaklığı, elektron yoğunluğu, etkin iyonlaşma derecesi ve plazmanın genişleme uzunluğu hakkında bilgi vermektedir. X-ray lazer için öncü Mo plazma oluşumunda kullanılan deney düzeneği ilerki çalışmalar için tasarlanmıştır.

Anahtar Kelimeler: Ni-benzeri Mo lazer ortamı, EHYBRID kod, Plazma,
Rezonans çizgileri

To My Parents

ACKNOWLEDGMENTS

I would like to express my deepest gratitude to my supervisor, Prof. Dr. Sinan Bilikmen for his guidance, criticism. His advices have been of great help in overcoming many of the difficulties which arose throughout my study.

I would like to send my sincere gratefulness to Prof. Dr. Arif Demir for his suggestions and comments during this study.

I would like to thank Dr. Elif Kaçar for many helpful discussions and suggestions on especially EHYBRID code and its analysis.

My special thanks go to Dr. Burak Yedierler for helpful discussions, advice and encouragement during this study.

For their moral, endless understanding and encouragement, special thanks to my roommates Elif Yurdanur and Mustafa Huş.

Special thanks go to Salur Kurucu and METU Laser Laboratory members for their suggestions, comments, and contributions.

The computational aid of Emre Taşçı is gratefully acknowledged.

I especially thank my parents and especially my dear brother, Ahmet İnce, for their endless love and care all through my life.

My deepest thanks go to my uncle M.D. Osman Refik Çetin for his endless supports and gorgeous advices.

TABLE OF CONTENTS

PLAGIARISM.....	iii
ABSTRACT.....	iv
ÖZ.....	v
DEDICATION.....	vi
ACKNOWLEDGMENTS.....	vii
TABLE OF CONTENTS.....	viii
LIST OF TABLES.....	xi
LIST OF FIGURES.....	xii
LIST OF SYMBOLS AND ABBREVIATION.....	xv
CHAPTER	
1. INTRODUCTION.....	1
2. BACKGROUND FOR X-RAY LASER STUDY.....	3
2.1 Review of X-Ray Lasers.....	3
2.2 Laser Produced Plasma (LPP) Physics.....	9
2.3 Plasma Equilibrium.....	12
2.3.1 Local Thermal Equilibrium (LTE)	13
2.3.2 The Coronal Equilibrium (CE)	14
2.3.3 The Collisional Radiative Equilibrium (CR).....	15
2.4 Absorption in the Plasma.....	16
2.4.1 Collisional Absorption.....	17

2.4.2 Resonance Absorption.....	18
2.4.3 Raman and Brillouin Scattering.....	19
2.5 Emission in the Plasma.....	19
2.5.1 Bound-Bound Transitions.....	19
2.5.2 Bremsstrahlung (free-free).....	22
2.5.3 Recombination Radiation (free-bound)	22
2.5.4 Collisional Absorption to Produce X-ray Laser	23
2.5.5 Collisional Recombination to Produce X-ray Laser.....	28
2.6 Spectral (Resonance) Lines and Types of Broadenings.....	29
2.6.1 Natural Line Broadening.....	30
2.6.2 Doppler Broadening.....	31
2.6.3 Stark Broadening.....	32
2.6.4 Instrumentational Broadening.....	32
3. THE CODES FOR MODELING RESONANCE LINES AND THE X-RAY MEDIA.....	33
3.1 Hydrodynamic EHYBRID Code.....	34
3.2 Calculation of Spectral Lines.....	37
3.3 Raytrace.....	39
4. EXPERIMENTAL DESIGN.....	40
4.1 Suggested Experiment Set-Up.....	40
4.2 Simulation Result and Discussion.....	43
5. CONCLUSIONS.....	55
REFERENCES.....	57

APPENDICES

A. Specifications for Turbo Pump	61
B. Specifications for Pulsed Laser.....	63
C. Specifications for CCD Camera.....	64

LIST OF TABLES

TABLES

Table 1 Wavelength of the electron collisional excitation soft x-ray lasers in Ne-like ions [6].....	26
Table 2 Wavelength of the electron collisional excitation soft x-ray lasers in Ni-like ions [6].....	27
Table 3 EHYBRID code working process.....	35
Table 4 Specifications for turbo pump Varian 551 TV navigator.....	61
Table 5 Specifications for CFR400 Pulsed Nd:YAG Laser.....	63
Table 6 Specifications for Andor XUV CCD camera.....	64

LIST OF FIGURES

FIGURES

Figure 1	Schematic diagram of the curved slab target [6].....	5
Figure 2	Schematic arrangement of the first x-ray holography was made by Trebes <i>et al.</i> [37].....	8
Figure 3	Different plasma regions are caused by the laser solid interaction.....	11
Figure 4	Spontaneous Emission, E_i and E_j are the energy levels, N_i and N_j are the density of these levels then A_{ji} is spontaneous emission rate.	20
Figure 5	Stimulated Emission, E_i and E_j are the energy levels, N_i and N_j are the density of these levels then B_{ji} is stimulated emission rate.....	21
Figure 6	Spontaneous Absorption E_i and E_j are the energy levels, N_i and N_j are the density of these levels then B_{ij} is spontaneous absorption rate.....	21
Figure 7	The simplified energy level diagram of Ne-like ion scheme [6].....	24
Figure 8	The simplified energy level diagram of Ni-like ion scheme [6].....	25
Figure 9	Hydrogen-like ion collisional recombination [6].....	29

Figure 10 Suggested Design of the Experimental Set-Up.....	41
Figure 11 The pulse shape used in the simulation.....	44
Figure 12 The theoretical Ni-like Mo and Co-like Mo resonance lines emissions spectrum.....	45
Figure 13 Efficient ionization degree versus distance at time 2.8 ns for all cell number. 14 is the maximum ionization degree at 5.09×10^{11} W/cm ² laser pulse intensity.....	46
Figure 14 Efficient ionization degree versus plasma distance for the cell number 79. Maximum efficient ionization degree is 14.....	46
Figure 15 Efficient ionization degree versus time (ns) at various focusing pulse power. * is 3.83×10^7 W, + is 2.83×10^7 W, ◆ is 1.83×10^7 W, — is 1.33×10^7 W, ▲ is 1.03×10^7 W, * is 1.00×10^7 W, ■ is 0.83×10^7 W	47
Figure 16 Electron density versus time graph for the cell which has the highest N _e value. Maximum N _e is 1.45×10^{22} cm ⁻³	48
Figure 17 Electron temperature versus time graph for the cell which has the highest T _e value. Maximum T _e is 73 eV.....	48
Figure 18 Electron density versus plasma distance at 3.8 ns. Maximum N _e is 1.45×10^{22} cm ⁻³	49
Figure 19 Electron temperature versus plasma distance at 2.6 ns. Maximum T _e is 73 eV.....	49

Figure 20 The ratio Co-like 4p-3d / Ni-like 4p-3d versus laser pulse intensity.....	50
Figure 21 Maximum temperature versus focusing laser pulse intensity for laser produced Mo plasma.....	51
Figure 22 Maximum electron density versus focusing laser pulse intensity for laser produced Mo plasma.....	52
Figure 23 The intensity of resonance lines versus time which gives a FWHM value at the 5.09×10^{11} W/cm ² laser pulse intensity.....	53
Figure 24 The intensity of resonance lines versus time at the 1.44×10^{12} W/cm ² laser pulse intensity.....	54

LIST OF SYMBOLS AND ABBREVIATIONS

$\Delta\nu_D$:Frequency FWHM for the Line Profile
A	:Atomic Number
Å	:Angstrom (10^{-10})
Ag	:Silver
C	:Carbon
c	:Speed of Light in Vacuum
CCD	:Charged Coupled Device
CE	:Coronal Equilibrium
C_{ji}	:Collisional Excitation Rate
Co	:Cobalt
CPA	:Chirped Pulse Amplification
CR	:Collisional Radiative
CRM	:Collisional Radiative Model
Cu	:Copper
D	:Dimension
Dy	:Dysprosium
E_i	:Energy Level
E_{ij}	:Energy Difference
E_j	:Energy Level
eV	:Electronvolt
f	:Femto (10^{-15})
FWHM	:Full Width at Half Maximum
Ge	:Germanium
H	:Hydrogen
h	:Planck's Constant
Hz	:Hertz
I	:Laser Irradiance
J	:Joule
k_B	:Boltzmann's Constant
KOU	:Kocaeli University

Li	:Lithium
LLNL	:Lawrence Livermore National Laboratory
LPP	:Laser Produced Plasma
LTE	:Local Thermal Equilibrium
Mo	:Molybdenum
n	:Nano (10^{-9})
N_c	:Critical Density
Nd	:Neodymium
Nd:YAG	:Neodymium-Doped Yttrium Aluminium Garnet
Nd-glass	:Neodymium-Doped Glass
Ne	:Neon
N_e	:Plasma Electron Density
Ni	:Nickel
N_i	:Density of Energy Level
N_j	:Density of Energy Level
p	:Pico (10^{-12})
Pd	:Palladium
Se	:Selenium
Sn	:Tin
T	:Escape Factor
Ta	:Tantalum
T_e	:Electron Temperature
Ti	:Titanium
W	:Watt
w_l	:Laser Light Frequency
w_p	:Plasma Frequency
α_{ib}	:Absorption Coefficient
ε	:Emissivity
ε_0	:Dielectric Constant
λ	:Laser Wavelength
μ	:Micro (10^{-6})

CHAPTER 1

INTRODUCTION

This work is concentrated on obtaining X-ray laser source from a plasma produced by focusing a pulsed laser beam on a solid target. Population inversions produced by collisional pumping and recombination pumping are the methods to achieve lasing at the x-ray wavelength. X-ray wavelength is between 1 Å and 400 Å. Collisional pumping is the process for achieving lasing action at the Nickel (Ni)-like Molybdenum (Mo) x-ray laser media. The initial observations of unsaturated x-ray lasing is created by using single pulses of nanosecond duration and nearly kilo joules of energy. Nowadays, experiments are increasingly aimed at decreasing the size of the pumping laser needed to achieve saturated lasing.

In chapter 2, the evolution of x-ray laser studies has been briefly reviewed. The physics of laser produced plasma (LPP) with their regions such as solid, shocked, ablation and coronal are summarized. Local thermal equilibrium (LTE), coronal equilibrium (CE) and the collisional radiative equilibrium (CR) which are the plasma equilibrium conditions are discussed. Laser energy absorption and emission in the plasma are mentioned. Then for the last part of this chapter spectral (resonance) lines and types of broadenings such as natural line broadening, Doppler broadening, Stark broadening and the other important type of broadening instrumental broadening are outlined.

In chapter 3, the codes used for modeling the x-ray media and resonance lines are mentioned. These codes are the hydrodynamic EHYBRID code and its post-processor Raytrace. Then some necessary calculations for spectral lines are given.

In chapter 4, detailed simulations of a preformed molybdenum plasma which is created by using Nd:YAG laser pulse with a pulse duration of 6 ns, pulse energy of 60 mJ and pulse intensity 5.09×10^{11} W/cm² at a wavelength 532 nm are undertaken using the EHYBRID code. X-ray resonance lines between 25 Å and 40 Å emitted from the molybdenum plasma have been performed. We can use the simulations to design the experiment easily because the input data for producing plasma can be calculated before the experiment. An experimental set-up design to produce preformed Mo plasma for x-ray laser is done for the future work.

CHAPTER 2

BACKGROUND FOR X-RAY LASER STUDY

2.1 Review of X-Ray Lasers

The first laser which is named maser with the microwave wavelength is invented at 1960s. After this invention the search started for laser which operates at different wavelengths especially at shorter wavelength. This was achieved by x-ray lasers which deliver quasi-monochromatic, partially coherent photons in the spectral range shorter than a few tens of nm [6]. There are several methods for producing x-ray lasing such as using a capillary discharge, a free electron laser or optical field ionization. In this work, x-ray lasing using a laser produced plasma is considered.

Amplified spontaneous emission at photon energies around 50 eV and operating at 20.6 nm and 20.9 nm was first demonstrated at the mid 1980s in Lawrence Livermore National Laboratory (LLNL). In this experiment, D. L. Matthews *et al.* used an optical laser ionized thin foils of selenium by collisional excitation to produce a population inversion of the $2p^53p$ and $2p^53s$ of the Neon (Ne)-like. The output of this experiment was highly anisotropic [27]. The theoretical groundwork for the experiments was given by Rosen *et al.* [23].

Most of the x-ray laser experiments depend on the collisional excitation process but in 1985 the first recombination type of soft x-ray laser was made at Princeton University. The recombination pumped process based on the rapid cooling of the plasma medium by free expansion causes rapid decrease of the electron density.

This type of expansion causes to obtain a nonuniform plasma medium and also difficulty to control cooling rate. To avoid these problems a novel method was investigated by Suckewer *et al.* proposed to use a strong solenoidal magnetic field and cooling by radiation losses. In this experiment a CO₂ laser was used as a pump laser. The plasma was created by using solid carbon as a source of plasma. The Hydrogen (H)-like Carbon (C) at 18.2 nm and 13.5 nm lasing signals were achieved. Although the mechanism of population inversion in this case was not clear, the result encouraged scientists [6].

The Nickel (Ni)-like amplifier is produced by a thin foil of Tantalum (Ta) with focusing a high intensity optical laser. This laser is NOVA which is the near infrared laser at LLNL. The heated foil then becomes plasma that expands to form a large, uniform gain medium. The largest gain was obtained with the population inversion between the levels $(3d_{3/2}4d_{3/2})_0 - (3d_{3/2}4p_{1/2})_1$ at 4.5 nm and a duration 250 ps with a gain 2.3 cm⁻¹. This is the first demonstration of an x-ray laser on short wavelength. This spectral region, whose name is water window, has a high resolution and high contrast ratio so we can see the biological specimen in water [25], [6]. Many scientists made such kind of studies.

X-ray laser, which occurs in the laser produced plasma expanding away from the solid surface due to electron collisional pumping has a wavelength shorter than 6 nm. This x-ray laser is achieved by R. Smith *et al.* In this experiment, the output of the Ni-like Dysprosium (Dy) laser at 5.86 and 6.37 nm, pumped by Nd-glass laser in the 75-ps double-pulse configuration at 2×10^{13} W/cm² peak intensity, is measured experimentally and studied theoretically using a rate equation and one-dimensional amplified spontaneous emission model [35]. Then, stimulated emission becomes a significant process to population inversion.

For the first time, T.N. Lee *et al.* used slab targets of Germanium (Ge) and Copper (Cu) as a plasma source and the result was soft x-ray laser at the wavelength of

19.5 and 28.5 nm. The lasing plasmas were produced by a driving laser beam at a wavelength of 1.05 μm and, the full width at half maximum (FWHM) 2 ns and energy of 600 J [21]. Use of slab targets has some limitations due to the x-ray refraction. The research group at the Osaka University suggested to use a curved slab target to compensate these limitations (Figure 1). Using such slabs increases the intensity and decrease the divergence of the x-ray laser beam [6].

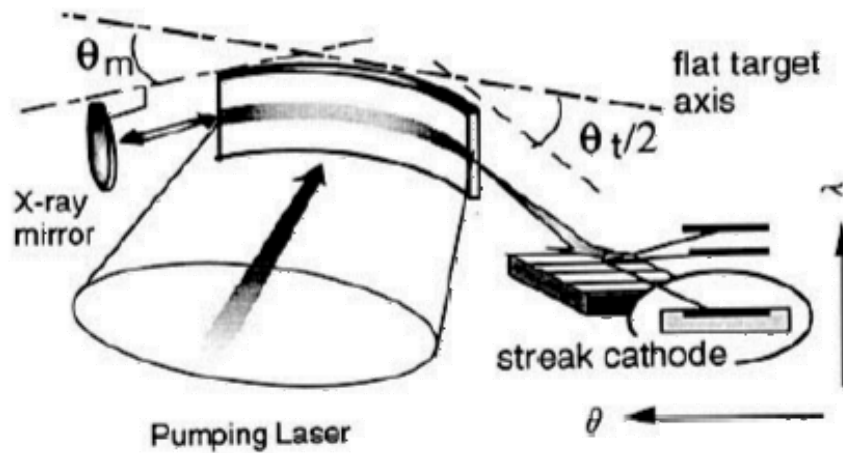


Figure 1: Schematic diagram of the curved slab target [6].

The next improvement was to use a pre-pulse to create a preplasma. J. Nilsen *et al.* reported an application of the pre-pulse technique which used a low intensity pre-pulse before the main optical drive pulse to prepare the plasma prior to lasing in low-Z, Ne-like ions [30]. The use of the pre-pulse technique increased the x-ray laser efficiency. Most researchers use some variations of the pre-pulse technique to achieve lasing in Ne-like or Ni-like ions. The technique of using a ns pulse to perform and ionize the plasma, followed by a ps pulse to heat the plasma has been realized for the first time by the study of P.V. Nickel *et al.* In this research, a nanosecond pulse creates a plasma of Ne-like ions of Titanium (Ti), followed by a

subpicosecond pulse which excites a nonstationary population inversion. With only a few joules of pump energy, a compact x-ray laser at 32.6 nm was achieved [29].

The aims of the x-ray laser research are to increase the energy of the x-ray photons, the intensity and the efficiency of the x-ray laser beam. Although a number of brilliant ideas for pumping the medium were investigated, the best idea is to use a very short optical laser for pumping. This recent work has shown that it is possible to use chirped pulse amplification (CPA) laser as a main pulse. Silver (Ag) and tin (Sn) slab targets were irradiated by focused CPA glass laser in the experiment of T. Kawachi *et al.* In this experiment, the laser pulses consisted of two pulses with 4 ps duration, separated by 1.2 ns. Strong amplification in the Ni-like Ag and Sn x-ray lasers at the wavelengths of 13.9 nm and 12.0 nm were archived. A hydrodynamics simulation coupled with a collisional radiative model was performed under the present experimental conditions, and the simulations result was compared with the experimental results [15].

Generating x-ray laser by using laser produced plasma especially Ni-like Molybdenum x-ray laser is mentioned here. Two developments improved the efficiency of these collisional pumped Ne-like and Ni-like ion x-ray lasers. The first which gives the better absorption of the main pulse is the pre-pulse technique where the pre-pulse has a low energy and a few nanoseconds. The second advance is the transient collisional excitation, where a nanosecond pre-pulse is followed by a short picoseconds pulse which pumps the population inversion. Recent work has further progress towards a high-repetition-rate soft x-ray laser based on longitudinal pumping with optical field ionization followed by collisional excitation. Nowadays, another method invented by R. Keenan which is also discussed below [16].

In the year 2000, J. Nilsen *et al.* used two pulse techniques for obtaining Ni-like Mo x-ray laser at a wavelength of 18.9 nm using the COMET laser at LLNL to

illuminate slab targets of Mo up to 1 cm length with a one joule, 600 ps pre-pulse followed 700 ps later by a five joule [31].

An obliquely incident beam (60°) which was also applied in the x-ray laser experiment was reported by R. Tomassini *et al.* Due to the use of this technique Ne-like Ti at and Ni-like Mo soft x-ray lasers are routinely realized using electron collisional excitation. In the experiment, laser pulses from the ATLAS Ti:sapphire laser, who are delivering energy of 300 mJ in 150 fs and 10 Hz repetition rate, are focused onto target by a gold-coated cylindrical mirror in obliquely incidence configuration. Then, wavelength at 18.9 nm and 22.6 nm lines in Ni-like Mo and wavelength at 32.6 nm line in Ne-like Ti were observed [38].

In few setups, the pre-plasma was created by a laterally incident beam while the heating pulse was directed nearly parallel to the target surface, along the axis of the plasma column [22], [32]. Longitudinally pumping 2 mm long Mo preformed plasma with high intensity 475 fs laser pulse duration, a highly directive soft x-ray laser at 18.9 nm wavelength is generated by the experiment of T. Ozaki *et al.* at NNT Basic Research Laboratory [32].

M. A. Loratonda *et al.* reported the characteristics of a saturated high-repetition rate Ni-like Mo laser at 18.9 nm. In the experiment, soft x-ray laser was pumped at a 5-Hz repetition rate by 8-ps 1-J optical laser pulses impinging at grazing incidence, which is a another method, into a precreated Mo plasma [20]. In the present example, J. Tümmler *et al.* demonstrated soft x-ray lasing at 18.9 nm with a repetition rate of 10 Hz obtained by a different set of pump parameters where a short (picoseconds) pulse irradiates a Mo plasma column generated by a long (a few hundred picoseconds) pulse [39].

R. Keenan *et al.* have demonstrated a 10 Hz Ni-like Mo x-ray laser operating at 18.9 nm with 150 mJ total pump energy by employing a novel pumping scheme. The grazing-incidence scheme is described, where a picosecond pulse is incident

at a grazing angle to a Mo plasma column produced by a slab target irradiated by a 200 ps laser pulse [16].

A great number of groups try to get extremely high brightness which means that a divergence of the x-ray beam is less than a few mrad with a narrow spectral band and a short-pulse duration which is a few ps. The main areas where the x-ray laser is used are x-ray laser holography, interferometer, radiography, and microscopy.

Holography which is a three dimensional imaging was first performed with the x-ray laser by Trebes *et al.* in 1987 using a Ne-like Selenium (Se) x-ray laser at a wavelength of 20 nm (Figure 2). Then other groups also tried to do x-ray holography with various x-ray wavelengths [6].

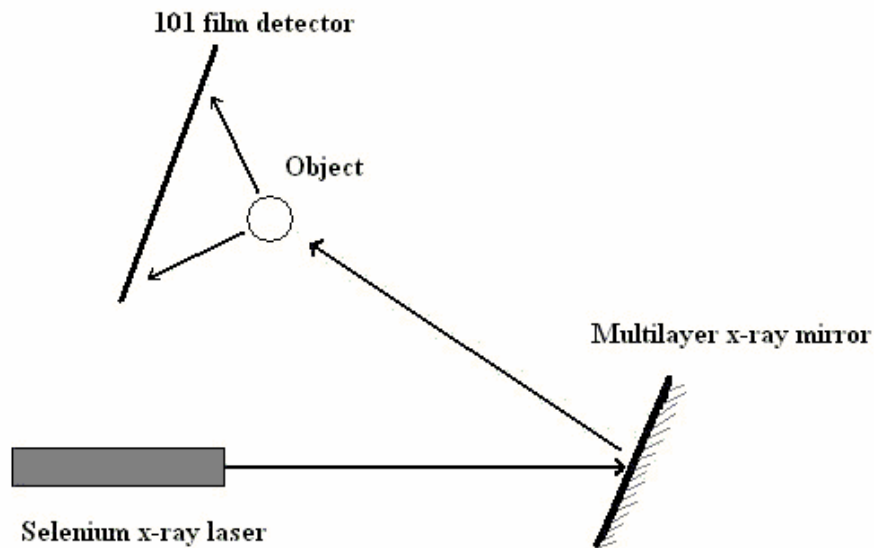


Figure 2: Schematic arrangement of the first x-ray holography was made by Trebes *et al.* [37].

X-ray laser interferometry can be used for measurements in material science, metrology and especially dense plasma diagnosis. In 1995, the first soft x-ray laser interferometry which is useful for probing large, high density and expanding plasmas was demonstrated by DaSilva *et al.* [37].

This type of laser provides high brilliance with extremely short-pulse duration which can apply to the observation of plasma using parameters radiography techniques. The short wavelength enables the x-ray laser to probe larger and higher density plasmas. [37]. Key *et al.* made an experiment on the plasma probing by an x-ray laser in 1995 [6].

X-ray microscopy is a method to observe microstructures by using a high-brightness short-pulse x-ray. In other words, x-ray microscopy needs directional, short pulse, high-intensity and monochromatic but incoherent beam. In 1992, DaSilva *et al.* carried out the first demonstration of soft x-ray laser microscopy [6].

It also has other useful applications such as observation of solid material luminescence in the ultraviolet spectral, producing low temperature highly ionized plasma although there is no evidence it is an attractive study [6].

2.2 Laser Produced Plasma (LPP) Physics

Producing free electrons and ions by focusing high power pulsed laser beams on solid targets is one of the most promising alternative methods to produce plasma which has a high temperature, and density. This plasma is also suitable to produce x-ray laser. The reason is the laser intensity I is proportional with the electric field as E^2 . The modest laser intensity produces easily electric fields which are clearly sufficient to remove electron on the solid target interface by ionization and heating by collisions.

Laser intensity is

$$I = \frac{1}{2} \epsilon_0 c n E^2 \quad (2.1)$$

where ϵ_0 is the dielectric constant, c is the speed of light in vacuum and n is the plasma refractive index [36]. This laser intensity is sufficient to produce enough electric field to remove electrons at the vacuum solid interface and these electrons accelerate with collision in the laser produced electric field and cause further ionization and heating [36], [17].

After a few hundred femtoseconds, significant number of ions is formed. Then laser light interacts predominantly with the free electrons in the produced plasma. As a result, produced plasma consists of certain regions such as solid, shocked, ablation and coronal region. As shown in figure 3, the properties of these regions are different from each other. For instance, coronal region when compared with the ablation region has a high temperature but lower density. The plasma density profile is diminishing exponentially along the plasma [8], [36].

The critical region gives the soft x-ray radiation or ultraviolet radiation which is the bound-bound transition. Using this laser solid interaction hard x-ray originates from the ablation region. The spectra of the x-ray photons are characterized by the electron temperature and electron density because of the collisions. Wavelength, intensity, pulse duration and the spot size of the laser beam define the x-ray propagation.

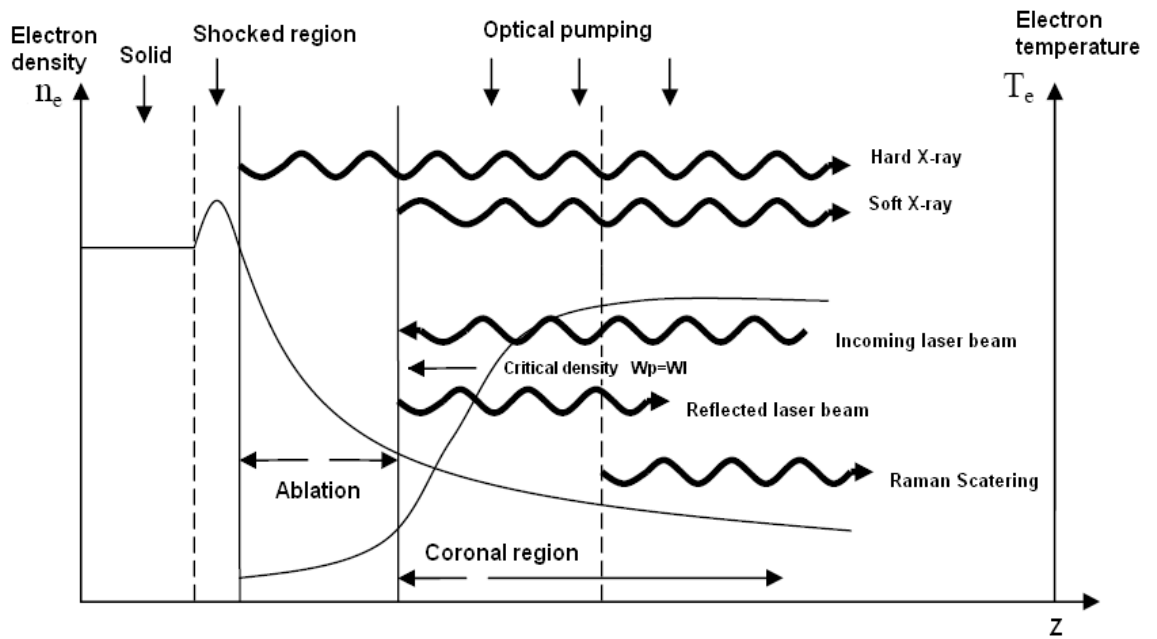


Figure 3: Different plasma regions are caused by the laser solid interaction.

The laser light can only penetrate up to critical density, where the natural oscillation frequency of the electrons relative to the plasma frequency equals the laser light frequency. Laser light frequency is given by

$$w_l = \frac{2\pi c}{\lambda} \quad (2.2)$$

here λ is the laser wavelength. Plasma frequency is equal to

$$w_p = \sqrt{\frac{N_e e^2}{m \epsilon_0}} \quad (2.3)$$

N_e is the plasma electron density, m is the electron mass and e is the electron charge and ϵ_0 dielectric constant [4].

Equalizing the plasma frequency with the laser frequency

$$\sqrt{\frac{N_e e^2}{m \epsilon_0}} = \frac{2\pi c}{\lambda} \quad (2.4)$$

we can find the critical density N_c ;

$$N_c = \frac{4\pi^2 c^2 m \epsilon_0}{\lambda^2 e^2} . \quad (2.5)$$

The laser beam is absorbed at electron densities up to the critical value at which the plasma frequency is equal to the laser frequency by inverse bremsstrahlung.

In generally, the x-ray laser experiment is undertaken by using two laser pulses, [29], [31], [32], one is the pre-pulse and the other one is the main pulse. In this type of experiment main laser interacts only with the plasma which is produced by the pre-pulsed one. The laser energy is almost completely absorbed by inverse bremsstrahlung, which is mentioned in the absorption in the plasma, in the sub-critical regions of the plasma when preformed plasma produced. At the critical region resonance absorption is the dominant absorption without collision [8].

2.3 Plasma Equilibrium

There are two main approximations to classify plasma for calculations and it is very important to know the domain of applicability of the three equilibrium models. These are local thermodynamic equilibrium (LTE), the coronal equilibrium (CE) and also another equilibrium condition is collisional radiative equilibrium (CR).

2.3.1 Local Thermal Equilibrium (LTE)

In generally, plasma calculations and measurements are based on the local thermodynamic equilibrium (LTE) assumption [11]. The main advantage of such an assumption is the simplicity of the formulas for ionization state densities and excited level population distributions [11]. LTE is characterized by the high density plasma where the collisional exciting and de-exciting processes completely dominate radiative exciting and de-exciting processes [11].

To apply LTE, there is a condition between the quantum states j and i which is

$$n_e C_{ji} \geq 10 A_{ij} \quad (2.6)$$

where A_{ij} is the radiative decay rate and C_{ji} is the collisional excitation rate [8].

In most laboratory plasmas, radiative absorption is weak because of the small size of the plasmas and so LTE conditions are valid. Substituting the value of the radiative decay rate and the collisional excitation rate in the equation 2.6 we have a criterion which is specified by Mc Whirter for applying LTE assumption that collisional processes are greater than the radiative ones [36]. This criterion is

$$N_e \geq 1.9 \times 10^{16} T_e^{1/2} E_{ij} \text{ cm}^{-3} . \quad (2.7)$$

In this assumption, N_e is the electron density measured in cm^{-3} and T_e is the electron temperature, E_{ij} is the energy difference between the two states. T_e and E_{ij} are measured in electronvolt. For LTE this criterion, or the other name is collision limit, must be satisfied [36].

In equilibrium, the ratio of the populations of the bound quantum states within a single ionization stage is determined by the Boltzmann ratio.

This ratio is independent from electron density N_e and depends on the electron temperature T_e

$$\frac{N_j}{N_i} = \frac{g_j}{g_i} \exp\left(-\frac{E_{ij}}{k_B T_e}\right) \quad (2.8)$$

where N and g are the population density and degeneracy, respectively, with j and i subscripts designating the respective upper and lower quantum states, k_B is Boltzmann's constant and E_{ij} is the energy difference between the two states [8]. This situation is valid for the collisional exciting and de-exciting processes are in equilibrium with radiative exciting and de-exciting processes.

Saha equation which is the ratio of the population of any two levels in ionization stages is given by

$$\frac{N(Z+1)n_e}{N(Z)} = 2 \frac{g(Z+1)}{g(Z)} \left(\frac{2\pi m_e k_B T_e}{h^2}\right)^{3/2} \exp\left(-\frac{X(Z)}{k_B T_e}\right) \quad (2.9)$$

here, $N(Z)$ and $g(Z)$ are the population density and degeneracy of the i^{th} quantum state in an ion with charge Z and $N(Z+1)$ and $g(Z+1)$ are correspondingly the population density and degeneracy of the j^{th} quantum state in an ion with charge $Z+1$. For the other parameters, $X(Z)$ is the ionization energy, h is the Planck's constant [8], [36]. The electron temperature can be estimated using the line ratio between two same ionization stages in this condition.

2.3.2 The Coronal Equilibrium (CE)

The coronal equilibrium (CE) state where the plasma is considered as optically thin has a low electron density at high temperatures so that exciting transitions are collisional and all de-exciting transitions are radiative [11].

Under these conditions ionization equilibrium is a balance between collisional ionization and radiative recombination [5]

$$N(Z)S(Z) = N(Z + 1)R_{rr}(Z + 1) \quad (2.10)$$

here, $S(Z)$ is the collisional ionization rate, $R_{rr}(Z+1)$ is the radiative recombination rate, $N(Z)$, $N(Z+1)$ are the ground level population densities of the Z -ionized and $(Z+1)$ -ionized ions [8].

Due to the low density plasma is optically thin and many photons escape before they can excite another atom and the only way for an upward transition is by collisions. Since collision rate depends on density which is low in CE, the only way for depopulation is by spontaneous emission. There is a criterion for to apply coronal equilibrium model that is given by

$$A_{ij} \gg n_e C_{ji} \quad (2.11)$$

C_{ji} is the collisional excitation rate coefficient and the A_{ij} is the spontaneous emission probability [8].

The intensity ratios of spectral lines are independent of the electron density because spectral line intensities depend only on the collisional excitation rates in coronal equilibrium. The coronal model is appropriate for tokamak plasmas [9].

2.3.3 The Collisional Radiative Equilibrium (CR)

In the collisional radiative equilibrium, only the highly excited states follow a Boltzmann distribution, whereas the lower levels follow a distribution typical of CE [11]. This system can be solved locally for given N_e and T_e values and also assuming that free electrons in the plasma have a Maxwellian velocity distribution

at a temperature T_e . This model is suitable for the high temperature and high density plasma [11].

In this type of equilibrium both of the collisional and radiative processes are effective on the excited ion or atom level density. Collisions change the level of density to affect the ratio of the radiative transitions which contribute the radiation on the plasma.

CR model can be coupled to a hydrodynamic code describing the plasma evolution. This can be done in a 0-dimensional code considering the particle, momentum and energy equations or in one of the large codes used in inertial confinement fusion work, in which all types of plasma transport and laser absorption phenomena can be included [7]. The simulations can be simplified for our interest in one of two ways. Firstly, the CR model can be handled as a post-processing of the hydrodynamic calculations. Secondly, ionization and radiation transport are handled in real time with a simplified model which is adequate to evaluate the effect of radiation on the overall hydrodynamic behavior [7].

2.4 Absorption in the Plasma

A laser beam propagates in the plasma until the critical region. As a result of this, absorption process in the different plasma region is different from each other. Collisional absorption occurs at the coronal region and resonance absorption is dominant at the critical region. There are also some other absorption mechanism such as Raman and Brillouin Scattering [17].

2.4.1 Collisional Absorption

Collisional absorption is the simplest and the reasonable way to absorb laser energy in a plasma and this process is also known as “*inverse bremsstrahlung*” [10]. The electrons oscillate at the laser frequency which is the result of the laser beam’s electromagnetic fields. The effect of the electric field dominates over the magnetic field and the electron oscillates with a velocity

$$v_e = v_{osc} \sin(\omega_l t) \quad (2.12)$$

here, ω_l is the laser frequency and this condition is valid only for the low laser intensities [10].

The absorption coefficient, or the inverse bremsstrahlung, α_{ib} calculated for typical laser is given by

$$\alpha_{ib} = \frac{\nu_{ei} \omega_p^2}{nc(\nu_{ei}^2 + \omega_l^2)} \quad (2.13)$$

where the ν_{ei} is the electron-ion collision frequency [36].

A simple model of the effect of the oscillations is obtained by imagining that the direction of motion of each electron which is randomized every electron collision time τ_e . The energy of oscillation becomes disordered at each collision and in this model each electron converts energy $(1/2)m_e v_{osc}^2$ to the thermal energy of the plasma every time τ_e . In other words, the volume of the plasma heating rate is

$$(1/2)n_e m_e v_{osc}^2 / \tau_e . \quad (2.14)$$

This energy is derived from the electromagnetic fields and therefore constitutes an absorption process which is especially effective for short wavelength [10].

2.4.2 Resonance Absorption

Resonance absorption is the laser energy absorption without collision. In critical region, laser frequency is equal to the plasma frequency so electromagnetic wave excites a plasma wave. If the laser light is not incident normally to the plasma density gradient at the critical region and the polarization of the laser light is in the plane of the angle of incidence and reflection, its energy can be best transferred to the plasma. This is called the “*p-polarization*” [36], [10]. Oblique waves are reflected from a point at a density $n_e \cos \alpha$ where α is the angle of incidence. The wave penetrates evanescently beyond the reflection point and can still excite a plasma wave at the critical surface [10]. When the polarization and the angle of incident match, plasma wave grows until some dumping process emerges.

Unfortunately, the small amounts of electrons absorb energy by resonance absorption and they become fast and hot. These energetic electrons distribute their energy uniformly so the inner part of the target is heated and cause some problem because of the high pressure at the center of the sample. This disadvantage can be diminished by keeping the laser intensity low and wavelength short. This combination causes the product $I\lambda^2$ to be small so the electron energy is low, and their mean free path is short so that the inner part of the target will not be heated. If the laser intensity can not be decreased, the wavelength must be reduced. A small wavelength increases inverse bremsstrahlung and this absorption gives the low energy to the electrons which are at the critical surface [10].

2.4.3 Raman and Brillouin Scattering

Assuming almost complete laser absorption does not give the good result when we compare the data with experimental outcome because there is an unmodeled laser energy. Possibilities include different laser scattering processes such as Raman and Brillouin scattering [17]. Raman scatter occurs up to the quarter critical density and produces an electron plasma wave and a scattered photon of half the laser frequency. Brillouin scatter produces regular density modulations in the plasma with period equal to the laser wavelength due to the formation of an ion acoustic wave [10].

2.5 Emission in the Plasma

Laser produced plasma emit x-ray basically in three ways. These are bound-bound transitions, Bremsstrahlung (free-free), and recombination radiation (free-bound). Initial and the final situation of the electron give the names of last two transitions. Here, collisional absorption and collisional recombination to produce x-ray laser will be discussed.

2.5.1 Bound-Bound Transitions

Bound-bound transitions occur between two ion energy levels, E_i and E_j , leading to line spectra. Other names of these transitions are spontaneous emission, stimulated emission and spontaneous absorption. These three types of transitions are given in the figures 4, 5, 6. In thermal equilibrium, the total rate of transitions from a lower level to higher level (figure 6) is equal to the rate of transitions from a higher level to the lower level (figure 4, 5).

The energy difference between two levels is given by

$$h\nu = E_i - E_j \quad (2.15)$$

here, h is the Planck's constant.

Figure 4 shows the spontaneous emission transition which has a rate coefficient “ A_{ji} ”. The Einstein coefficient of this type of radiation named by spontaneous emission rate is

$$A_{ji} = \frac{8\pi^2 e^2 h \nu_{ji}^3 g_i}{m_e c^3 (4\pi\epsilon_0) g_j} f_{ij} \quad (2.16)$$

here, ν_{ji} is the transition frequency, g_i and g_j are the blackbody radiation distribution and f_{ij} is the oscillator strength. This coefficient depends upon the energy and the wavefunctions of the emitting ions [5], [8], [10], [24]. These three bound-bound transitions are in equilibrium.

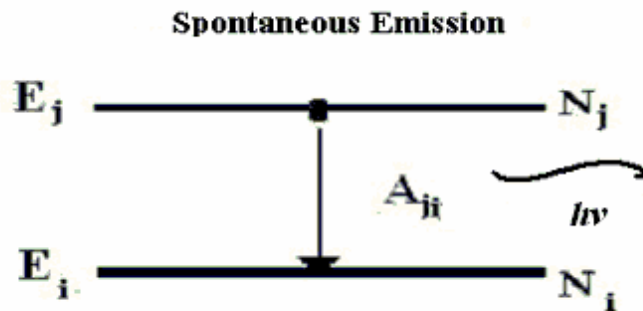


Figure 4: Spontaneous Emission, E_i and E_j are the energy levels, N_i and N_j are the density of these levels then A_{ji} is spontaneous emission rate.

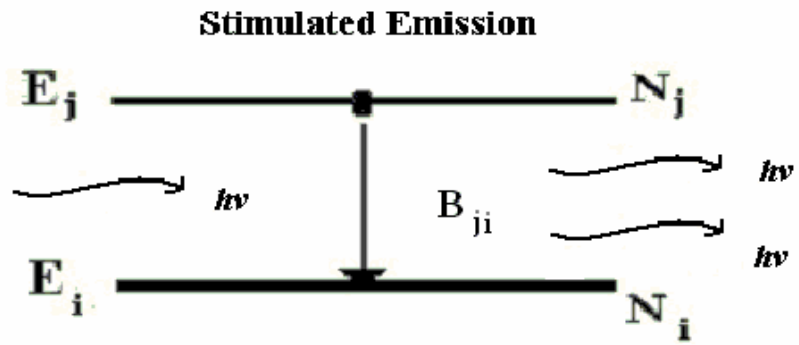


Figure 5: Stimulated Emission, E_i and E_j are the energy levels, N_i and N_j are the density of these levels then B_{ji} is stimulated emission rate.

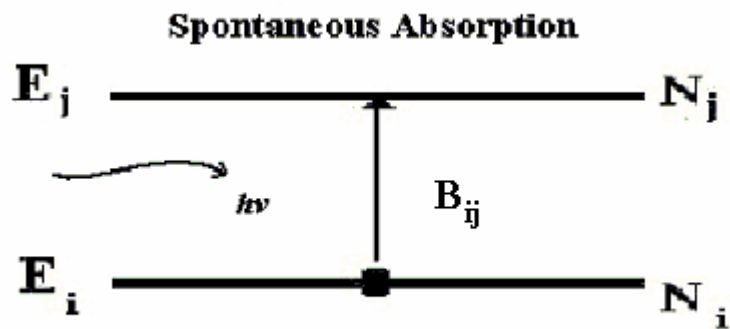


Figure 6: Spontaneous Absorption E_i and E_j are the energy levels, N_i and N_j are the density of these levels then B_{ij} is spontaneous absorption rate.

The line shape of the spectra is influenced by the natural lifetime of the transitions between the two states and the motion of the emitting ion and its interaction with the plasma [24].

2.5.2 Bremsstrahlung (free-free)

Free-free radiation which is the simplest type occurs between two free energy levels. This process is caused by the acceleration of the charged particles in the Coulomb field of other charged particles [5].

2.5.3 Recombination radiation (free-bound)

Free-bound radiation occurs when a free electron recombines with an ion. This recombination radiation which occurs in the coronal region of the plasma has a three operations. Names of these operations are radiative recombination, two body recombination and three body recombination. Recombination into state gives



In this process, energy of the photon can be calculated by adding the kinetic energy of the electron, which has a mass m and velocity v , to energy difference between levels [5]

$$h\nu_{ji} = E_{\infty} + \frac{1}{2}mv^2 - E_i \quad (2.18)$$

In two body recombination, a free electron is caught by the ion but this reaction is radiationless transition. At the same time the electron in the last orbital of this ion becomes excited. Then this excited ion emits energy while it is turning back to initial level [17].

As the last operation called three body recombination which is a collisional process occurs when two free electron collide with an ion [5].

Three body recombination is represented by



In the recombination process, electron temperature is rapidly changing, so it is the basic principle of production to x-ray wavelength [10].

2.5.4 Collisional Absorption to Produce X-ray Laser

In the equilibrium plasma, ions have specific number of electrons such as H-like (2), Ne-like (10), Ni-like (28) and Palladium (Pd)-like (46). These ions can survive in a wide range of temperature and density.

To produce x-ray laser there exists two main processes. One is collisional excitation, or collisional absorption, and the other one is recombination. X-ray lasers which are obtained by Ne-like and Ni-like ions are pumped by collisional excitation process in the laser produced plasmas. Figure 7 and 8 show the transitions respectively Ne-like and Ni-like simplified energy level diagram. By recombination pumping method H-like and Lithium (Li)-like x-ray lasers are produced [6].

In 1976, Zherikhin *et al.* first described a mechanism for obtaining an inversion between Ne-like ions. The Ni-like scheme, proposed firstly by Maxon *et al.* in 1985 has proven to be successful for short wavelength amplification below 10 nm at LLNL [6].

Collisional excitation is occurred by the upper levels which are predominantly excited by direct electron impact collision from the ground state of the ion stage of interest. The first successful demonstration of lasing at soft x-ray wavelengths utilizing this approach was realized at LLNL [34].

In 1987, Ni-like soft x-ray lasers were first demonstrated. Firstly, Hagelstein proposed the use of low Z Ni-like ions to develop table-top collisional lasers with the wavelengths near 20 nm [6]. For several years the maximum amplification obtained in Ni-like ions remained smaller than that obtained in Ne-like systems, and below the values required for gain saturation. Table 1 and table 2 show the wavelength from the Ne-like and Ni-like soft x-ray lasers which were observed experimentally [6].

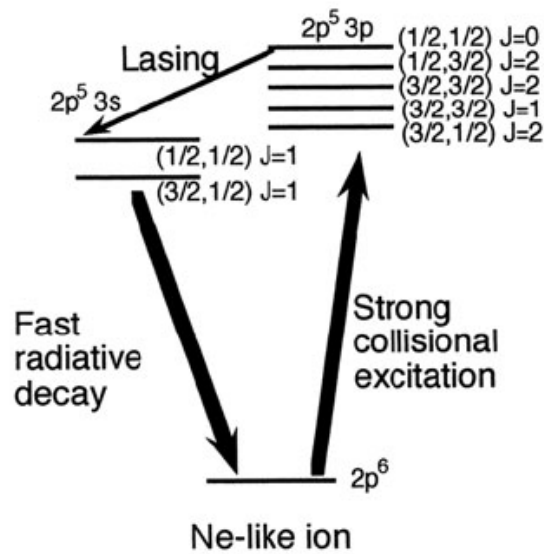


Figure 7: The simplified energy level diagram of Ne-like ion scheme [6].

Nevertheless, the use of multiple-laser-pulse excitation techniques and the optimization of target geometries have greatly increased the gain in Ni-like ions. The amplification of soft x-ray radiation by collisional excitation is not limited to Ne-like and Ni-like ions. Gain has also been observed in Cobalt (Co)-like ions and Neodymium (Nd)-like ions [34].

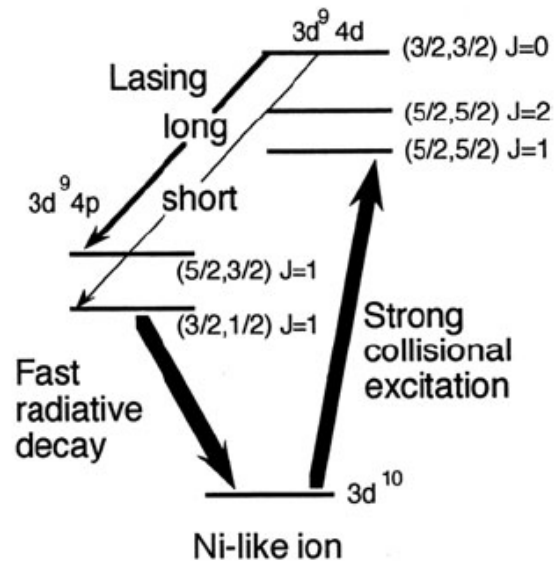


Figure 8: The simplified energy level diagram of Ni-like ion scheme [6].

Table 1: Wavelength of the electron collisional excitation soft x-ray lasers in Ne-like ions [6].

Atomic number and symbol of the Element	Wavelengths (nm)	Scheme	Reference
$_{47}Ag$	9.9365, 10.0377	Ne-like	Fields <i>et al</i> 1992
$_{42}Mo$	10.64, 13.10, 13.27	Ne-like	MacGowan <i>et al</i> 1987b
$_{41}Nb$	13.86, 14.04, 14.59	Ne-like	Nilsen <i>et al</i> 1993a
$_{40}Zr$	15.04	Ne-like	Nilsen <i>et al</i> 1993a
$_{39}Y$	15.5	Ne-like	Da Silva <i>et al</i> 1993
$_{38}Sr$	15.98, 16.41, 16.65,	Ne-like	Keane <i>et al</i> 1990
$_{37}Rb$	16.50, 17.35, 17.61	Ne-like	Nilsen <i>et al</i> 1992
$_{34}Se$	18.2, 20.6, 20.9	Ne-like	Nilsen <i>et al</i> 1995b
$_{32}Ge$	19.6, 23.2, 23.6	Ne-like	Daido <i>et al</i> 1995b
$_{30}Zn$	21.2, 26.2, 26.7	Ne-like	Rus <i>et al</i> 1997
$_{25}Mn$	22.1, 26.9	Ne-like	Li <i>et al</i> 1996a
$_{22}Ti$	32.63	Ne-like	Nilsen <i>et al</i> 1993b
$_{20}Ca$	38.3	Ne-like	Li <i>et al</i> 1995c
$_{14}Si$	87.4	Ne-like	Li <i>et al</i> 1997

Table 2: Wavelength of the electron collisional excitation soft x-ray lasers in Ni-like ions [6].

Atomic number and symbol of the Element	Wavelengths (nm)	Scheme	Reference
${}_{79}\text{Au}$	3.56	Ni-like	MacGowan <i>et al</i> 1992
${}_{74}\text{W}$	4.32	Ni-like	MacGowan <i>et al</i> 1992
${}_{73}\text{Ta}$	4.48	Ni-like	MacGowan <i>et al</i> 1992
${}_{72}\text{Hf}$	4.65	Ni-like	Daido <i>et al</i> 1999b
${}_{70}\text{Yb}$	5.609, 5.026	Ni-like	MacGowan <i>et al</i> 1988
${}_{67}\text{Ho}$	5.63, 6.20	Ni-like	Daido <i>et al</i> 1999b
${}_{66}\text{Dy}$	5.85, 6.41	Ni-like	Daido <i>et al</i> 1999b
${}_{65}\text{Tb}$	5.9, 6.7	Ni-like	Daido <i>et al</i> 1997
${}_{64}\text{Gd}$	6.33, 6.86	Ni-like	Daido <i>et al</i> 1999b
${}_{63}\text{Eu}$	6.583, 7.100	Ni-like	MacGowan <i>et al</i> 1987a
${}_{62}\text{Sm}$	7.36, 6.85	Ni-like	Daido <i>et al</i> 1999b
${}_{60}\text{Nd}$	7.92	Ni-like	Daido <i>et al</i> 1999b
${}_{59}\text{Pr}$	8.2	Ni-like	Daido <i>et al</i> 1997
${}_{58}\text{Ce}$	8.6	Ni-like	Daido <i>et al</i> 1997
${}_{57}\text{La}$	8.9	Ni-like	Daido <i>et al</i> 1997
${}_{54}\text{Xe}$	9.64, 9.98	Ni-like	Lu <i>et al</i> 2002

Table 2: Continued

Atomic number and symbol of the Element	Wavelengths (nm)	Scheme	Reference
$_{52}\text{Te}$	11.1	Ni-like	Daido <i>et al</i> 1997
$_{50}\text{Sn}$	11.97	Ni-like	Lin <i>et al</i> 1998
$_{49}\text{In}$	12.58	Ni-like	Lin <i>et al</i> 1998
$_{48}\text{Cd}$	13.17	Ni-like	Li <i>et al</i> 1998
$_{47}\text{Ag}$	13.89	Ni-like	Li <i>et al</i> 1998
$_{46}\text{Pd}$	14.68	Ni-like	Li <i>et al</i> 1998
$_{42}\text{Mo}$	18.90	Ni-like	Li <i>et al</i> 1998
$_{41}\text{Nb}$	20.33	Ni-like	Li <i>et al</i> 1998
$_{40}\text{Zr}$	22.02	Ni-like	Li <i>et al</i> 1998
$_{39}\text{Y}$	24.01	Ni-like	Li <i>et al</i> 1998
$_{36}\text{Kr}$	32.8	Ni-like	Sebban <i>et al</i> 2001b

2.5.5 Collisional Recombination to Produce X-ray Laser

The other method for x-ray laser is the collisional recombination process which is first proposed by Gudzenko and Shelepin in 1965. This type of process is the inverse of collisional electron ionization. Here, the atoms populate energy levels higher than the excited bound levels where the laser action occurs with the

collision of two free electrons. Figure 9 gives H-like ion collisional recombination. As the reaction above suggests, the collisional recombination rate is proportional to the square of the electron density. The recombination rate is also extremely sensitive to the electron temperature therefore; the generation of large population inversion by recombination requires a dense and relatively cold plasma [34], [14].

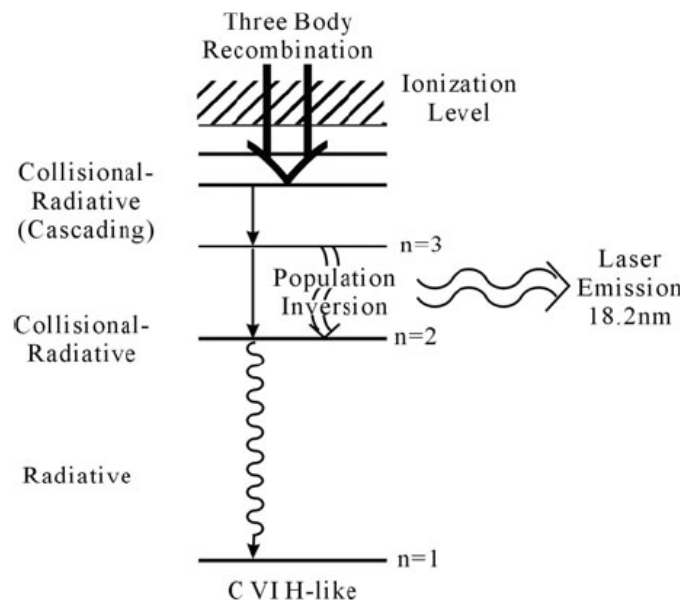


Figure 9: Hydrogen-like ion collisional recombination [6].

2.6 Spectral (Resonance) Lines and Types of Broadenings

A spectral line is important because its shape gives information about the emitting atom or ion in the plasma. A detailed analysis of the observed line shapes can give information about the density and temperature of the plasma.

If the plasma is optically thin the profile of the observed radiation will be the same as the emission line profile [5]. There are several possible mechanisms of line broadening in plasma, natural broadening, Doppler broadening, Stark broadening and instrumental broadening are important broadening mechanisms in a laser produced plasma. Here these broadening types are reviewed.

2.6.1. Natural Line Broadening

Natural line broadening is usually very small compared to other causes of broadening [5]. This broadening effect is described by a Lorentzian profile.

Lorentzian line shape

$$f_L(\nu) = \frac{2}{\pi(\Delta\nu_L)} \frac{1}{1 + (4\nu^2/(\Delta\nu_L)^2)} \quad (2.20)$$

where $\Delta\nu_L$ is the frequency FWHM or the line profile [36]. $\Delta\nu_L$ is equal

$$\Delta\nu_L = (1/2\pi)(\sum_i A_{ui} + \sum_i A_{li}) \quad (2.21)$$

The summations are over all lower energy states from the upper u and lower l states associated with the transition [36].

The equation 2.22 is valid when l is the ground state and upper level u can only decay to the ground state [36].

$$\Delta\nu_L = A_{ul}/2\pi \quad (2.22)$$

2.6.2 Doppler Broadening

This type of broadening is the change in frequency and wavelength of a wave that is perceived by an observer at rest relative to the atoms or ions which has a velocity. If the source gets closer to the observer at rest, the wavelength decreases and frequency increases. If the source moves away from an observer at rest, wavelength increases and frequency decreases. This condition is given by

$$\lambda = \lambda_0 \left(1 \pm \frac{v}{c} \right) \quad (2.23)$$

where λ is the wavelength calculated by an observer at rest, λ_0 is the wavelength of the source which has a velocity v and c is the speed of light in vacuum.

In a plasma, if the ion velocity distribution in a plasma is Maxwellian doppler broadening due to the different thermal motion of ions produces a Gaussian line shape which can be written as [36]

$$f_D(v) = \frac{2(\ln 2)^{1/2}}{\sqrt{\pi}(\Delta\nu_D)} \exp\left(-4 \ln 2 \frac{v^2}{(\Delta\nu_D)^2}\right) \quad (2.24)$$

here the $\Delta\nu_D$ is the frequency FWHM for the line profile. The value $\Delta\nu_D$ of is determined by

$$\Delta\nu_D = 2(\ln 2)^{1/2} \frac{1}{\lambda} \left(\frac{m}{2k_B T_i} \right)^{1/2} \quad (2.25)$$

where, T_i is the ion temperature in a plasma, m is the mass of the emitting ions and k_B is the Boltzmann's constant [36].

2.6.3 Stark Broadening

The possible main mechanism of line broadening is only pressure broadening which is named Stark broadening [5]. This type of broadening includes the effects of collisions with neutrals particles, resonance interactions between identical particles, and collisions with charged particles. The effects of collisions with neutral particles and resonance interactions between identical particles are important only in a weakly ionized plasma. For a highly ionized, high-density plasma, the effect of collisions with charged particles is most important because a strong electric field resulting from charged particles produces a broadening of the transitions between the split atomic levels. The broadening associated with these micro electric fields [26] as mentioned above is proportional to the ion and electron density in a plasma, electric field and also low plasma temperature. Stark broadening line profile is Lorentzian shape.

2.6.4 Instrumentational Broadening

Instrumentational line broadening is caused by the spectrometer. In this broadening, the entrance slit width, the beam size, the target width and also charged-coupled device (CCD) pixel size are important. This means that this type of broadening is depend on the experimental set-up. In many cases the instrumental profile can be approximated to a Gaussian profile without committing any important error [26].

CHAPTER 3

THE CODES FOR MODELING RESONANCE LINES AND THE X-RAY MEDIA

The simulations for modeling resonance lines and the x-ray media are very useful for predicting data to be used in the experiment easily. These codes also help us to evaluate experimental results of the laser produced plasmas. Yet, the codes are programmed for the variety of plasmas by different groups of people especially interested in x-ray laser. There are different codes such as hydrodynamic code and analytic code. They have different assumptions and calculations of plasma modeling. The names and properties of these codes are given below.

EHYBRID, LASNEX, MEDUSA, ICF3D are hydrodynamic codes. ICF3D used for high temperature plasma modeling is a three dimensional code. LASNEX which is developed at the Lawrence Livermore Laboratory is a “one dimensional Lagrangian code”. Another 1D Lagrangian code MEDUSA developed at Rutherford Appleton Laboratory differs from other 1D codes by using the average atom modeling for the calculation of the excited state number density. The 1.5-D hydrodynamics/atomic physics code is EHYBRID [14].

FLY, RATION, TRANSPECT, CRModel are the analytic codes but they have some differences. For example, FLY depends on time but RATION is time-independent. FLY was originally a 1D code but after some improvements on FLY, it has turned to a 3D collisional-radiative model. FLY, RATION, TRANSPECT and CRModel are collisional-radiative models but CRModel is used for calculating number density of the atomic levels in low temperature plasma [14].

RAYTRACE and B3DRTX give the information about the output X-Ray Laser beam [14]. In this part of the study Ehybrid code and its postprocessor Raytrace will be described.

3.1 Hydrodynamic EHYBRID Code

The simulations presented in this thesis are performed with the 1.5-D hydrodynamics/atomic physics code and sometimes called as quasi-2D, EHYBRID [33]. This code has been developed at the University of York by Geoff J. Pert with the help of his graduate students over the years [19]. This EHYBRID code is used by several groups simulating the x-ray laser media which is formed by laser solid target interaction. The design of experiments is easily performed by using this fluid simulation model because the input data for producing plasma can be calculated before the experiment. Expanded EHYBRID code details are given by Holden *et al.* [13]. In this work EHYBRID code will be reviewed.

The slab target is typically divided into 98 Lagrangian cells in the direction parallel to the incoming pump laser. The code solves the fluid equation of continuity and the Navier–Stokes equation to calculate the density profile in the pumping laser direction for 98 Lagrangian cells [1]. The fluid is hence modeled in this driving laser direction, which are assumed to be isothermal in each cell and the expansion of the transverse dimension is assumed to be self-similar [19], [12].

In this EHYBRID code, the laser beam is assumed to have a Gaussian profile at the target surface with a variable FWHM independent of the target size [28]. FWHM of the pulse duration, the length, the power of the laser pulse, and width and thickness of the target information are adequate to have an information about electron temperature, electron density, efficient ionization degree, plasma

expansion distance and resonance lines spectra of the element. Table 3 gives a summary of the EHYBRID simulation process.

Table 3: EHYBRID code working process

EHYBRID CODE WORKING PROCESS		
	Laser	Target
INPUT VALUES	Wavelength	Width
	Pulse Power	Length
	Pulse Duration	Thickness
	Focal Width	Atomic Data
	Focal length	
POSTPROCESSOR	The equation of state package Chart D	
	Inverse Bremsstrahlung	
	Resonant absorption	
	The thermal conductivity of the ions	
	The thermal conductivity of the electrons	
	The emissivity ϵ of spectral lines	
	Line intensities	
OUTPUT VALUES	RAYTRACE	
	Electron temperature	
	Electron density	
	Efficient ionization degree	
	Plasma expansion distance	
	Resonance lines spectra of the element	
Gain Coefficient		

The equation of state package Chart D has been incorporated into EHYBRID for the nuclear “ionic” terms [12]. This includes bonding of the solid at low temperatures and high densities, and tends to approximate the perfect gas in the limits of high temperatures and low densities. The implementation of an improved equation of state is necessary to stop the unphysical expansion of the cold slab without laser heating in the delay between the pre and main pulses which can give a misleading description of the plasma at the beginning of the main pulse [12].

In this computational model, absorption of the pumping laser is due to inverse Bremsstrahlung and resonant absorption at the critical surface are calculated [12], [19]. For resonance absorption, a fraction of 30%, of the laser energy reaching the critical density is dumped into the critical density cells and the remainder of the energy is reflected back into the low-density region for possible further inverse Bremsstrahlung absorption. As inverse Bremsstrahlung absorption is high, the assumed energy dump at critical level has only a small effect on the overall laser energy absorption. Radiative energy losses through recombination, Bremsstrahlung emission, and line emission processes are taken into account [2].

The thermal conductivity of both the ions and electrons is given by the classical Spitzer expressions, but the latter is subject to a flux limit $f = 0.1$. In the low temperature and the solid-density region there are some modifications. It should be noted that these modifications have negligible effect in single-pulse simulations because they only operate in a low-temperature regime [12].

Lateral energy transport may move energy from the lasing plasma region to heat the solid target beyond the focal region. Foil target can be used to eliminate this kind of losses. But also there is some incoherency when comparing the results predicted by simulation codes with experimental observations. This simulation must give correct data because of the validity of a code. The EHYBRID code does not explicitly model laser scatter and parametric processes which may be expected to be important with such long scale-length plasmas. This code has involved the

assumption of an f -factor [36]. Using the correction factor, $f \leq 1$, which is used to multiply the experimental laser energy to correctly simulate experimental observations [2].

3.2 Calculation of Spectral Lines

EHYBRID code simulates the spectral line of the plasma to do this it calculate some basic plasma parameters using some equations. These calculations are emissivity, line intensities and Doppler line width.

The emissivity ε of spectral lines at a particular time is calculated using [1]

$$\varepsilon = \sum N_i A_{ij} \frac{hc}{\lambda_0} dV \quad (3.1)$$

where N_i is the upper state population for a given transition, A_{ij} is the radiative transition probability for the transition, h is Planck's constant, c is the vacuum speed of light, λ_0 is the spectral line wavelength, dV is the volume of each cell and the summation is over the EHYBRID cells. The original EHYBRID code was modified to calculate the spontaneous transition rates A_{ij} from the absorption oscillator strengths used in the evaluation of the ionization balance [1].

The emissivity calculated using equation 3.1 is equivalent to the radiation intensity produced if the plasma is optically thin. Resonance lines are often optically thick as they have strong oscillator strengths. Opacity is modeled through an approximate escape factor based on the Holstein function for Doppler broadened lines [1]. Line intensities are evaluated in a post-processor to EHYBRID using the simulated N_i population densities and escape factor T [14].

$$T = \frac{1}{K_0 D \sqrt{\pi \ln(K_0 D)}} \quad \text{for } K_0 D \geq 2.5 \quad (3.2)$$

and

$$T = e^{-K_0 D / 1.73} \quad \text{for } K_0 D < 2.5 \quad (3.3)$$

In these two escape factor calculation K_0 is the absorption coefficient or the other name opacity of the resonance lines and D is the length of the plasma [14].

We can calculate the K_0 with the following equation [24]

$$K_0 = \frac{A_{ji} \lambda_{ij}^3}{8\pi c} n_i \frac{\lambda_{ij}}{\Delta\lambda} \left(1 - \frac{g_j n_j}{g_i n_i} \right) \quad (3.4)$$

where c is the light speed in the vacuum, g_i and g_j lower and upper statistical weight $\Delta\lambda$ is the Doppler line width [24]

$$\frac{\Delta\lambda}{\lambda_d} = 2\sqrt{2 \ln 2} \sqrt{\frac{2k_B T}{Mc^2}} = 7.70 \times 10^{-5} \sqrt{\frac{T}{A}} \quad (3.5)$$

where M , A and T being the mass number, the atomic number and the temperature of the emitting ion, respectively [24].

The intensity I_{tot} of resonance lines at a particular time are calculated using [1]

$$I_{tot} = \sum N_i \frac{hc}{\lambda_0} T A_{ij} dV \quad (3.6)$$

where N_i is the upper state population for a given transition. A_{ij} is the radiative

transition probability for the transition, h is Planck's constant, c is the vacuum speed of light, λ_0 is the spectral wavelength, V is the volume of each cell and the summation is over the EHYBRID cells [1].

3.3 Raytrace

RAYTRACE is a postprocessor to EHYBRID code, and can provide data on the nature of the output x-ray laser beam such as the x-ray laser beam divergence and output energies [1]. This means that it is used to generate experimental observations such as near and far field laser profiles. The 3D RAYTRACE code was developed and derived from an earlier 1D model by Toft [1], [13].

Defining the plasma variables as a rectangular grid, each cell of the plasma is divided into two triangular cells for the purposes of ray-tracing. The refractive index gradients which are defined by the densities at the cell corners are assumed constant in the cell. Ray paths are parabolic in constant refractive index gradients and the total ray path is calculated as a smooth sequence of parabolic arcs between the cell faces [13].

The plasma is assumed to be uniform along the lasing axis. This limits the accuracy of codes when calculating x-ray laser output parameters, where the gain changes significantly on time scales less than the transit time of the targets used. The static plasma implies that the raytrace code will correctly model a traveling-wave experiment but will increasingly overestimate the output of a laser as the gain time reduces below the transit time for the target [28]. The combination of EHYBRID and raytrace code has been used successfully in the model Ne-like and Ni-like ions with a traveling wave pump [18].

CHAPTER 4

EXPERIMENTAL DESIGN

4.1 Suggested Experimental Set-Up

The aim of this experimental set-up is to produce x-ray laser source from plasmas produced by focusing pulsed laser beams on a solid target. In such plasmas electron density ($N_e 10^{20}$ - 10^{23} cm^{-3}) and electron temperature ($T_e 10^2$ - 10^3 eV) are as high as the values that are enough to produce x-ray radiation.

The foreseen experimental set-up design in the laser produced Mo plasma consists of a vacuum chamber, a stage carrying the sample, a gate delay generator, a Nd:YAG laser, and charged-coupled device (CCD) detector for x-ray wavelength and a computer for control and data acquisition. Figure 10 gives the configuration design of this experimental set-up.

In the design, the target is placed in a stainless steel vacuum chamber which is vacuumed by turbo pump Varian 551 TV navigator. The specifications of this turbo pump are given in the Appendix A. This vacuum chamber has a volume of 0.59 m^3 . The vacuum chamber allows us easily to place the samples and lenses and also it has BK7 windows for directing the laser light onto the target. The vacuum chamber was mounted on an adjustable frame for changing the direction of the beam.

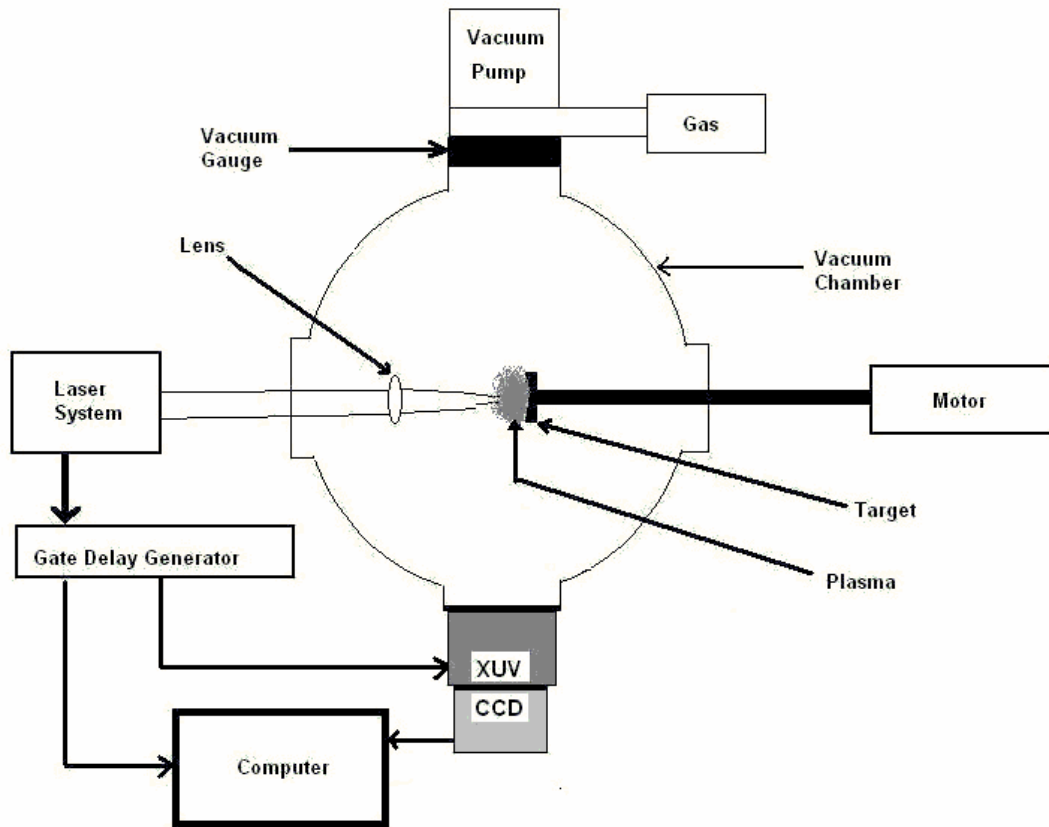


Figure 10: Suggested Design of the Experimental Set-Up

Gate delay generator is used to give a time interval between two laser beams those are applied to produce such a plasma and also this programmable timing generator is used to control the delay time between the laser pulse and the imaging system. This delay time between laser pulse and the imaging system is necessary because the plasma formation originate soon after the laser pulse interacts with the surface of the sample.

The laser must generate pulses of sufficient power to produce the plasma. The most widely used lasers are the Nd:YAG laser with output wavelengths of 1064 nm and the second harmonic of the Nd:YAG laser with 532 nm and pulse length of 5–10 ns. In this experiment, Mo plasma in a stainless steel vacuum chamber is planned to be produced by irradiating Mo slab with laser beam from the Big Sky

Laser CFR 400 Nd:YAG laser at the Middle East Technical University (METU) Laser Laboratory. Nd:YAG laser with a 230 mJ laser pulse energy at the fundamental wavelength of 532 nm, a 6 ns pulse duration, and 10 Hz repetition frequency is planned to be used in this experiment. The properties of this laser are mentioned in the Appendix B. The pulse was incident along the horizontal target length.

The XUV CCD recorded emission from x-ray region wavelength in the horizontal direction (perpendicular to the target surface). The collection angle of the XUV CCD in the vertical direction is limited by the entrance slit. The plume imaging is done by using Andor Model XUV CCD camera which has 1024×256 pixels. The width of the timing slit of the CCD was set to be 26 μm. In order to eliminate undesirable wavelength reaching the camera, a filter will be used. Further details and an accurate characterization of CCD detector devices can be found in Appendix C.

To determine the best pump pulse configuration for obtaining Ni-like Mo and Co-like Mo resonance lines for the Mo plasma, a series of shots using various pulse intensities are simulated using the EHYBRID code. After carrying out a few simulations the suitable inputs for the suggested experiment were found. Then figures of the simulation results and discussion part were sketched by using Microsoft excel.

When this laser pulse is focused by an appropriate lens on the solid surface, the resulting intensity is on the order of 5.09×10^{11} W/cm² which is sufficient to produce a plasma on solid Mo sample. The laser beam was overlapped onto the target in a 50 μm diameter focus by using converging lens to produce a peak intensity of the main pulse on the target of up to 5.09×10^{11} W/cm². Plasma emission begins on the target surface soon after the laser photons reach the surface of the target. The sample used in this simulation was pure Mo solid compound (99%) which is 25 mm in length, 25 mm in width and 1.0 mm in thickness.

This experimental set-up will be used for a comparison of the temporarily resolved resonance lines emissions from the Ni-like Mo and also Cobalt (Co)-like Mo pumped with nanosecond pulse with the predictions for the same emission from the hydrodynamic code EHYBRID.

In general, a laser is focused onto the sample surface, forming plasma at this surface. Laser produced plasma spectroscopy can be used for analyzing the resonance lines directly. The investigation of resonance lines is important for a number of reasons. Firstly, by observing the resonance-line emission to the ground state of the respective ion stages, we can appoint the relative abundance of the various ions present and the electron temperature. Secondly, ratios of the line intensities from different ion species are a standard technique for detecting information about the plasma. These ratios tend to be sensitive to changes with the electron temperature (T_e) and the electron density (N_e) [3].

4.2 Simulation Result and Discussion

In this simulation, a laser pulse with a 60 mJ energy at the wavelength of 532 nm and 6 ns pulse duration was focused on a Mo slab target to produce a plasma. The target is assumed 25 mm long flat slab consisting of 25 mm width and 1.0 mm thickness. The focusing laser beam diameter is 50 μm and its intensity is equal to 5.09×10^{11} W/cm². The pulse shape used in this experiment is shown in figure 11.

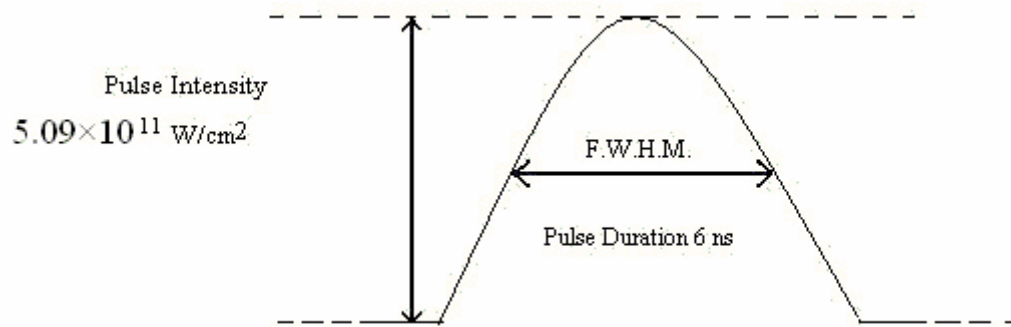


Figure 11: The Pulse shape used in the simulation.

A spectrum simulated with the EHYBRID code using $5.09 \times 10^{11} \text{ W/cm}^2$ pumping pulse intensity with a 6 ns pulse duration at 532 nm wavelength. Figure 12, the intensity versus wavelength diagram shows Ni-like and Co-like resonance lines emissions spectrum were calculated between 25 Å and 40 Å in this Mo plasma simulation. This figure shows that the Ni-like resonance lines intensities are weaker than the Co-like resonance lines intensities in this Mo laser produced plasma at $5.09 \times 10^{11} \text{ W/cm}^2$ pulse intensity.

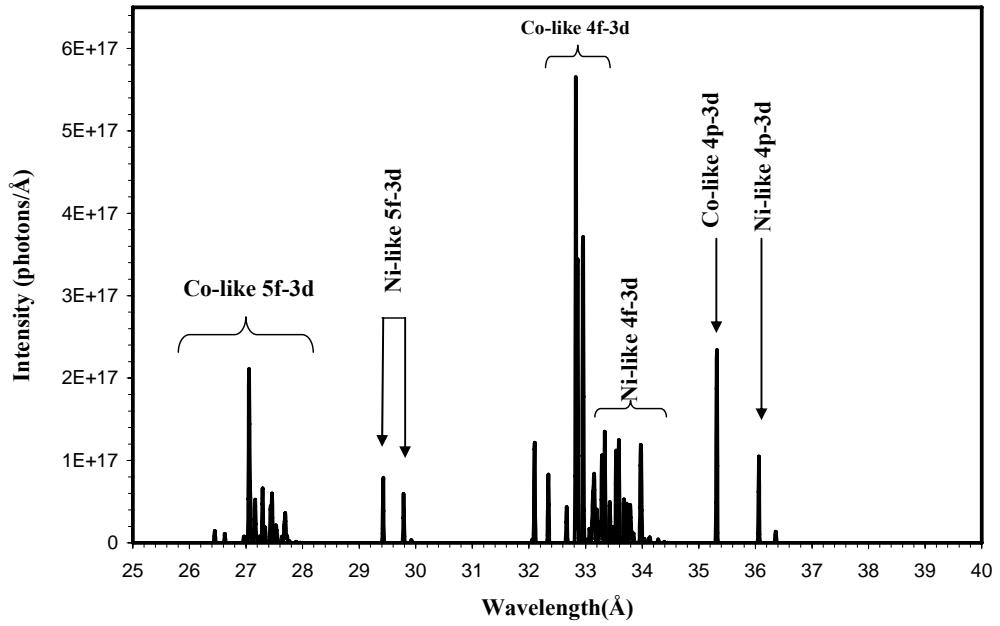


Figure 12: The theoretical Ni-like Mo and Co-like Mo resonance lines emissions spectrum.

Using the output of the Ehybrid code we also have an idea about the efficient ionization degree at the various pulse intensities. The efficient ionization degree gives which types of transition are archived in the plasma such as Ni-like and Co-like. If the ionization degree of the plasma is suitable for former transition in the plasma medium there has been sufficient number of ions that can produce Ni-like x-ray lasing. Figure 13 and figure 14 show the efficient ionization degree versus plasma distance for all cell at time 2.8 ns and the efficient ionization degree versus plasma distance for the cell number 79 at 5.09×10^{11} W/cm² laser pulse intensity, respectively.

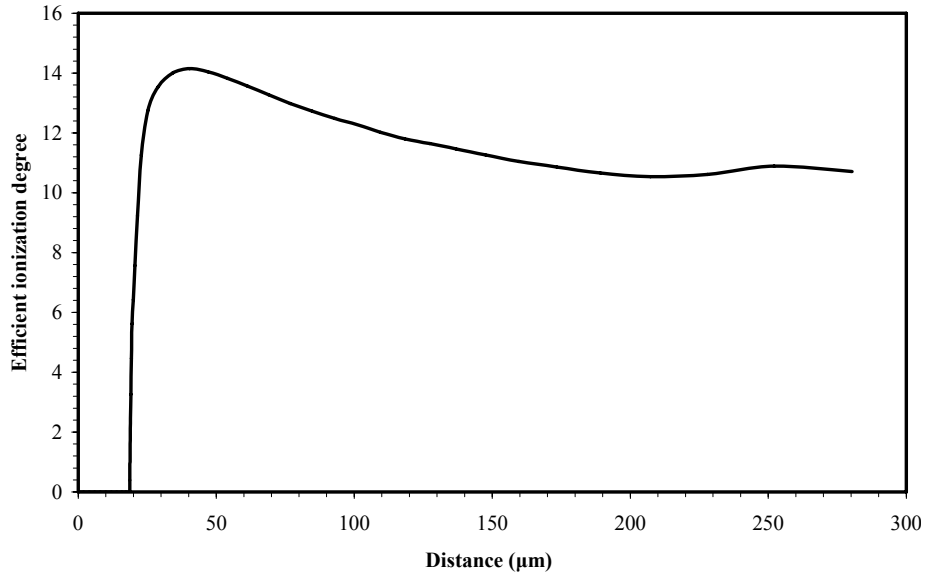


Figure 13: Efficient ionization degree versus distance at time 2.8 ns for all cell number. 14 is the maximum ionization degree at 5.09×10^{11} W/cm² laser pulse intensity.

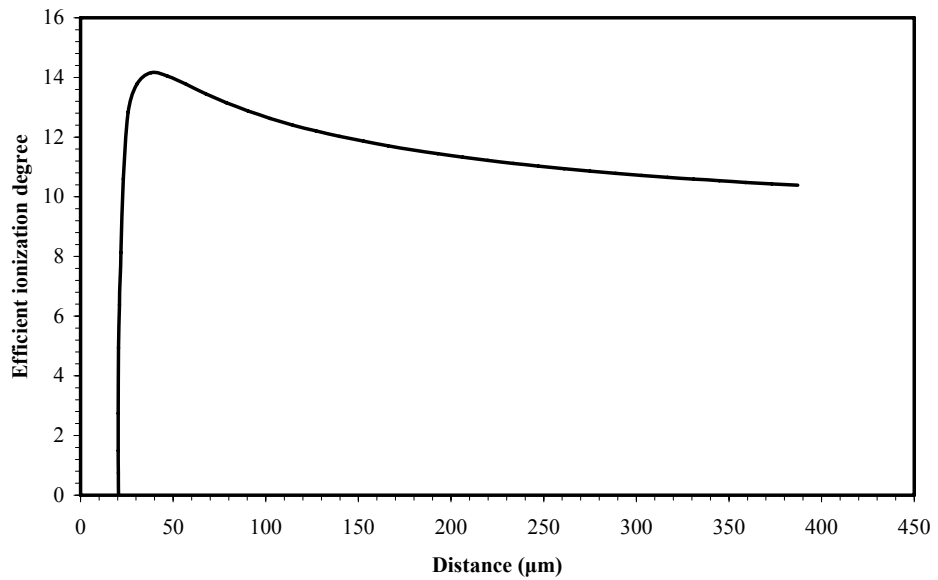


Figure 14: Efficient ionization degree versus plasma distance for the cell number 79. Maximum efficient ionization degree is 14.

Efficient ionization degree is changed by focusing laser pulse intensity. When the pulse intensity increases maximum ionization number also increases so they are directly proportional. The maximum ionization number is 14 for the cell number 79 at the laser beam intensity 5.09×10^{11} W/cm². Figure 15 shows the changing efficient ionization degree value with respect to the power of the laser beam.

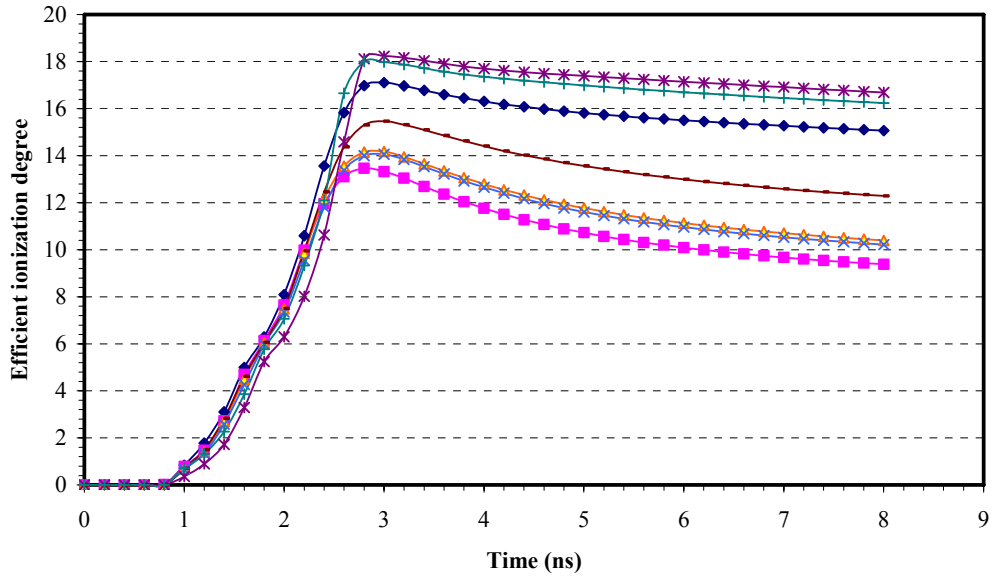


Figure 15: Efficient ionization degree versus time (ns) at various focusing pulse power. * is 3.83×10^7 W, + is 2.83×10^7 W, ◆ is 1.83×10^7 W, — is 1.33×10^7 W, ▲ is 1.03×10^7 W, *- is 1.00×10^7 W, ■ is 0.83×10^7 W.

Electron temperature and electron density were calculated in the Ni-like and Co-like Mo plasma by using EHYBRID code. Figure 16 and figure 17 show electron density and electron temperature versus time, respectively. These graphs describe the highest value of the electron temperature and the electron density of the Mo plasma. Figure 18 and figure 19 show electron density versus plasma distance at 3.8 ns and electron temperature versus plasma distance at 2.6 ns.

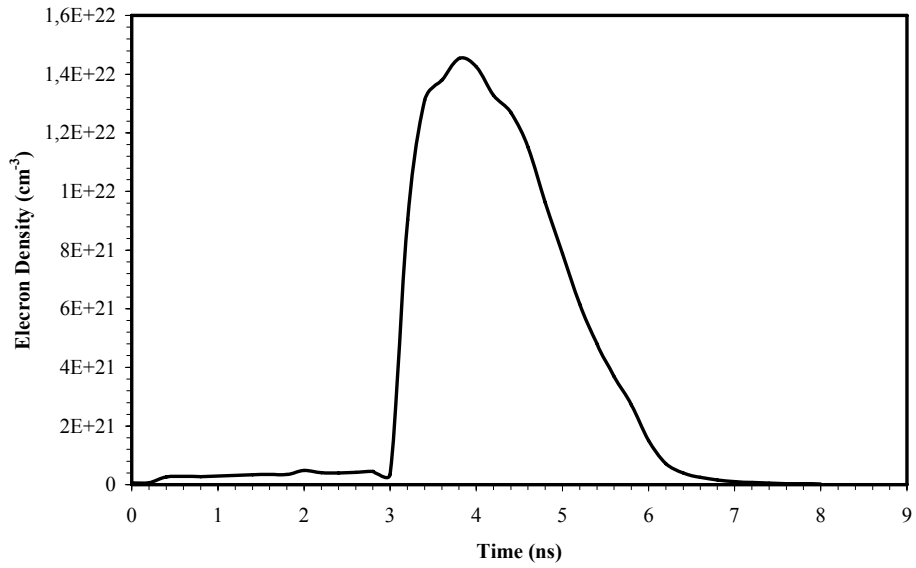


Figure 16: Electron density versus time graph for the cell which has the highest N_e value. Maximum N_e is $1.45 \times 10^{22} \text{ cm}^{-3}$.

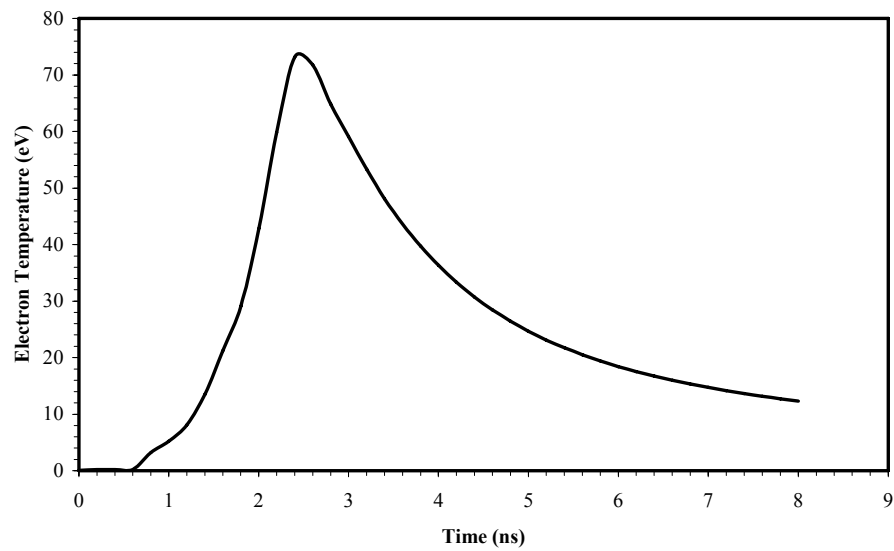


Figure 17: Electron temperature versus time graph for the cell which has the highest T_e value. Maximum T_e is 73 eV.

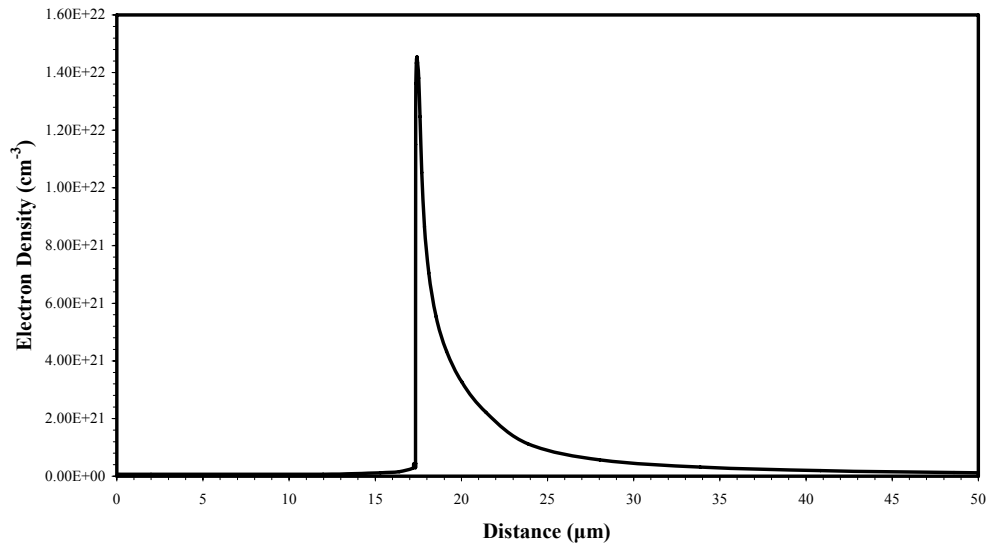


Figure 18: Electron density versus plasma distance at 3.8 ns. Maximum N_e is $1.45 \times 10^{22} \text{ cm}^{-3}$.

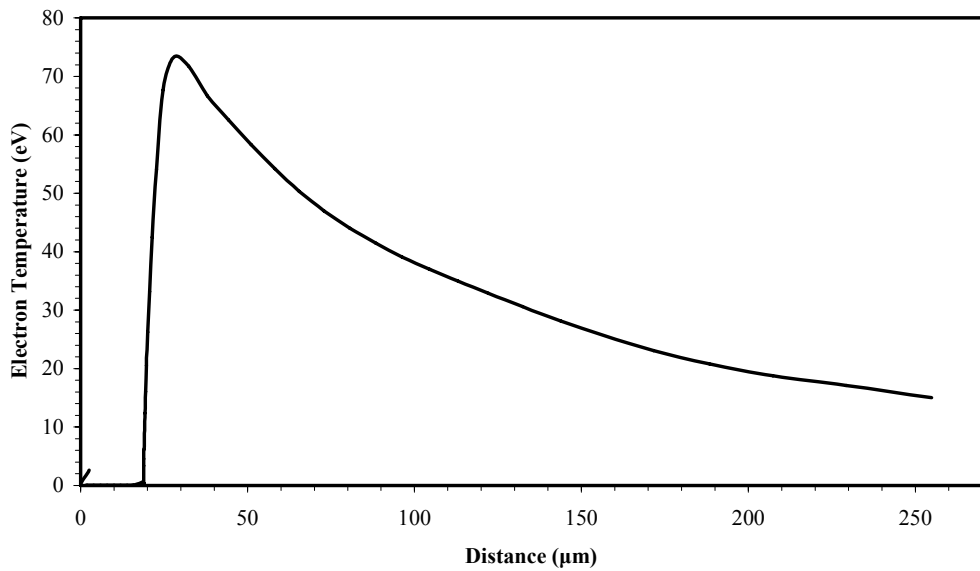


Figure 19: Electron temperature versus plasma distance at 2.6 ns. Maximum T_e is 73 eV.

The laser beam can only penetrate up to a critical density and the laser energy is almost completely absorbed by inverse bremsstrahlung, or collisional absorption, in the sub-critical regions. Using the equation 2.5, critical density for Nd:YAG laser was found and it is equal to $3.95 \times 10^{21} \text{ cm}^{-3}$. Thus the x-ray radiation depends on the collisional absorption so electron temperature and electron density are important for this process. Last four figures show that the maximum electron density is $1.45 \times 10^{22} \text{ cm}^{-3}$ and the maximum electron temperature is 73 eV.

The peak values of the resonance lines emissions depend on the pulse intensities of the focusing laser. Using the resonance lines spectrum for different laser pulse intensity we can calculate the line ratio which gives information about the electron temperature of the plasma. The comparison of the simulation results with the experimental results gives the electron temperature of the plasma. Figure 20 shows the ratio of Co-like 4p-3d to Ni-like 4p-3d versus different pumping laser pulse intensities.

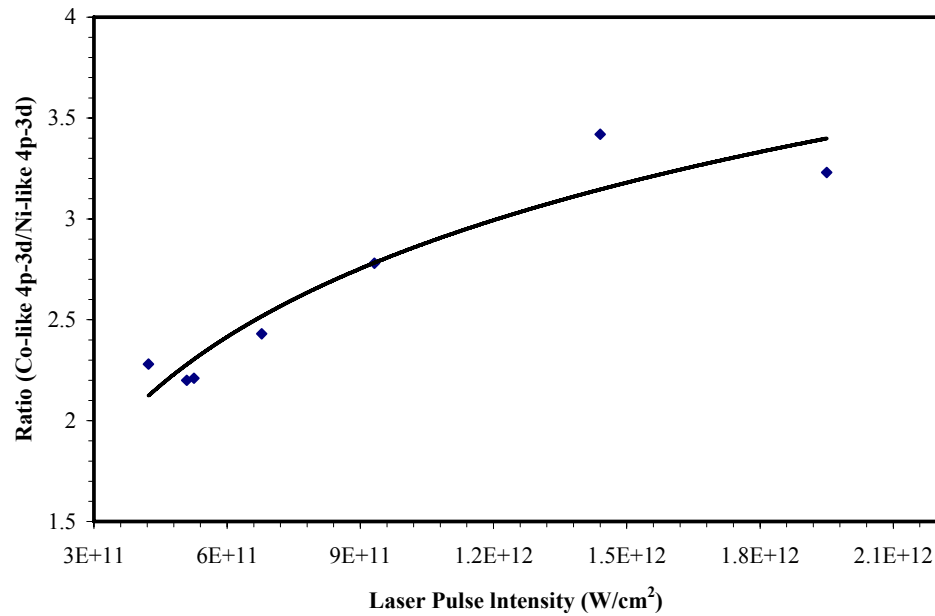


Figure 20: The ratio Co-like 4p-3d / Ni-like 4p-3d versus laser pulse intensity.

Electron temperature to the laser produced Mo plasma can be estimated using the line ratio. The maximum electron temperature versus laser pulse intensity for Mo plasma is shown in the figure 21. If the laser pulse intensity is known electron temperature of the plasma can be estimated by using this electron temperature versus laser pulse intensity graph.

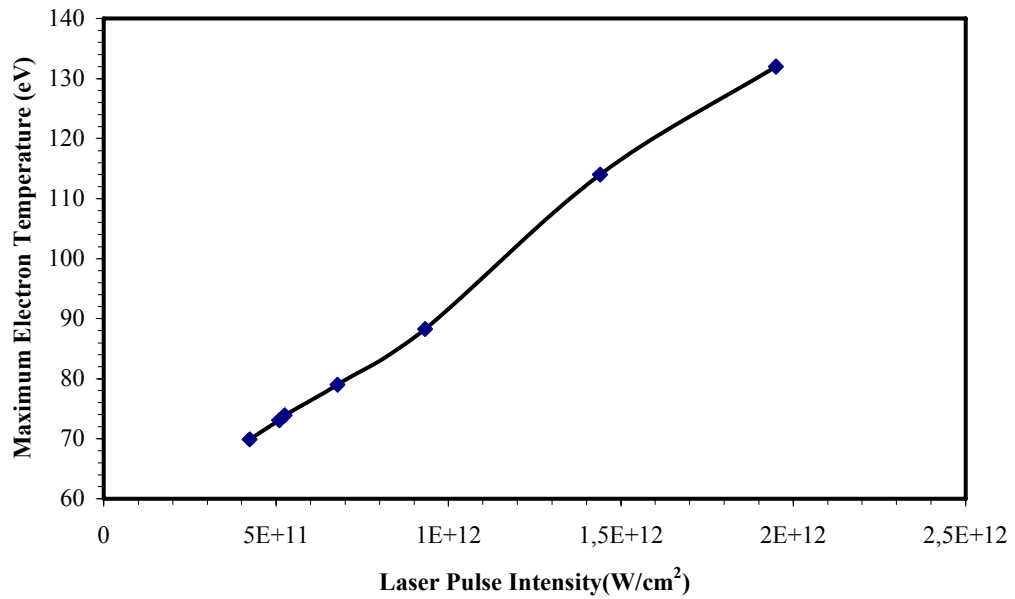


Figure 21: Maximum temperature versus focusing laser pulse intensity for laser produced Mo plasma.

The electron density can be estimated by using the laser pulse intensity like electron temperature. For this process maximum electron density versus laser pulse intensity graph is used. Figure 22 gives electron density versus laser pulse intensity for laser produced Mo plasma.

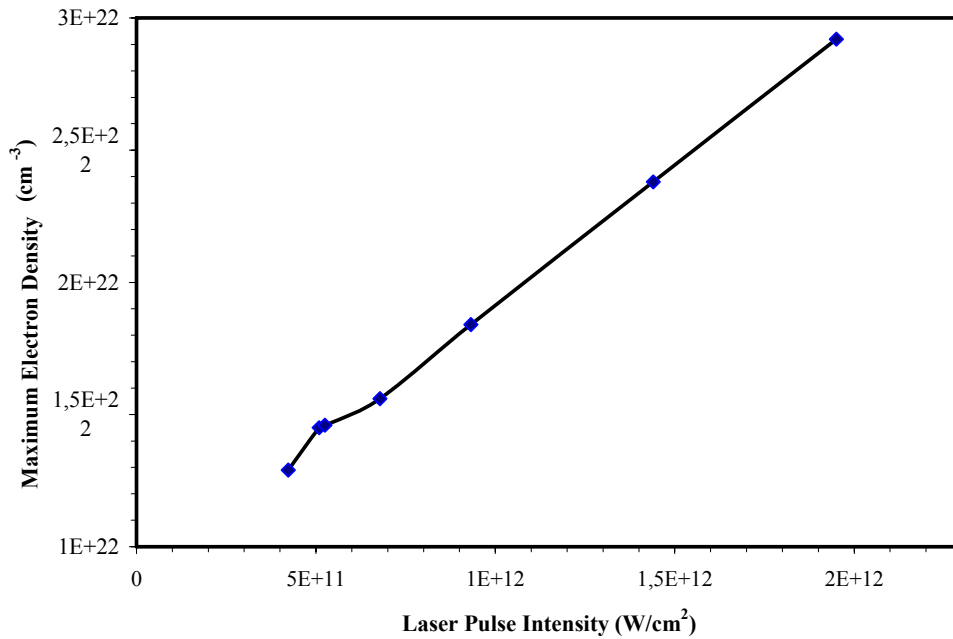


Figure 22: Maximum electron density versus focusing laser pulse intensity for laser produced Mo plasma.

Figure 23 shows the photon number versus time graph which gives a FWHM value at the $5.09 \times 10^{11} \text{ W/cm}^2$ laser pulse intensity. In this simulation FWHM is 2.6 ns. X-ray line emission time depends on the FWHM this means that the duration of the x-ray line emission increases when the FWHM increases. The graph in figure 23 has a Gaussian shape and when the focusing laser pulse intensity changes; this shape of the line also changes. Figure 24 gives this changing shape at the photon number versus time graph when pumping laser pulse intensity is $1.44 \times 10^{12} \text{ W/cm}^2$.

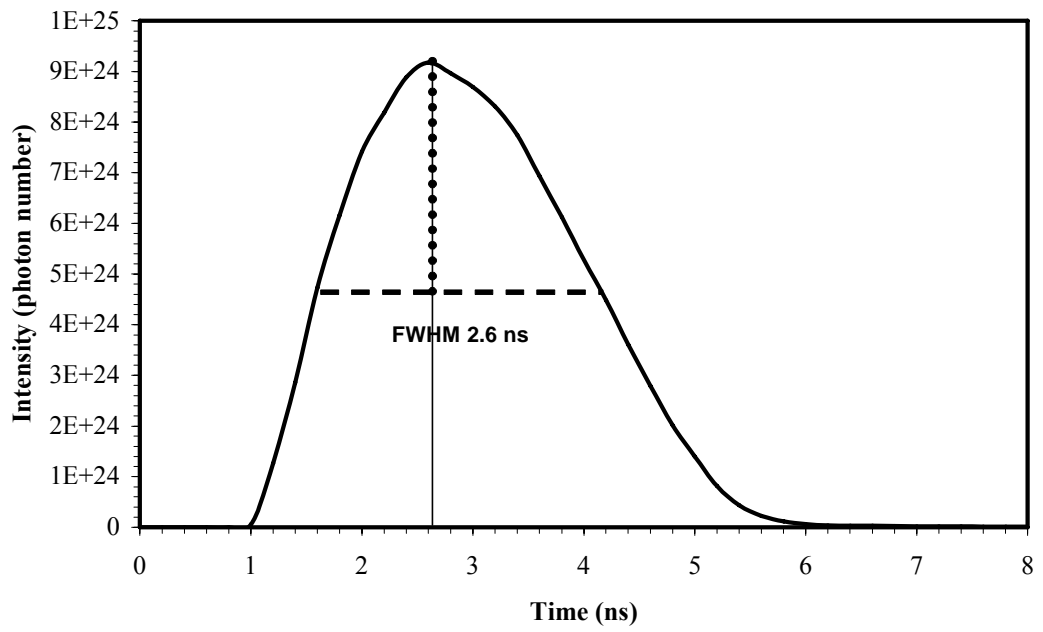


Figure 23: The intensity of resonance lines versus time which gives a FWHM value at the 5.09×10^{11} W/cm² laser pulse intensity.

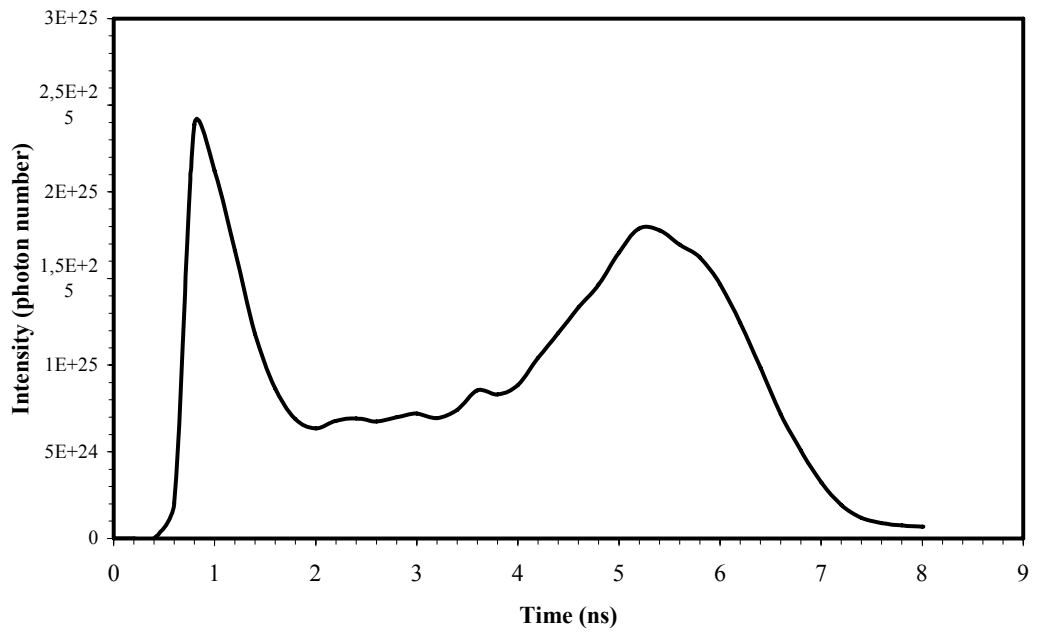


Figure 24: The intensity of resonance lines versus time at the $1.44 \times 10^{12} \text{ W/cm}^2$ laser pulse intensity.

CHAPTER 5

CONCLUSIONS

Ni-like Mo x-ray laser media is modeled using the EHYBRID code and its post-processor. The required atomic data for EHYBRID are obtained by using another code named Cowan. In this work, preformed Mo plasma simulation is done by using a Nd:YAG laser pulse with a 60 mJ energy, 532 nm wavelength and 6 ns pulse duration. Emitted x-ray resonance lines, Ni-like Mo and Co-like Mo, between 25 Å and 40 Å from the molybdenum plasma have been simulated by EHYBRID code which is based on a collisionally radiative model. The simulations for modeling resonance lines and the x-ray media are necessary for predicting input and output data for the experiment, easily. For example, resonance line emission from different ion stages has been used to monitor the plasma electron temperature. In the EHYBRID code, FWHM of the pulse duration, pulse length, the power of the laser pulse, and width and thickness of the target are sufficient to have an information about, electron density, efficient ionization degree and plasma expansion distance of the target. Making use of this code, various diagrams for laser produced preformed plasma of Ni-like Mo x-ray laser media in chapter 4 were drawn and from these diagrams we have gotten an information about the efficient Mo plasma parameters.

This work will be used for comparison of simulations with measurements of x-ray laser output and resonance line intensities and it has been shown to be useful in understanding the physics of x-ray lasing. Comparison of simulation results with the experimental results will become possible when our suggested experimental set-up design in this work is established. The agreement between model and experimental results will be good and suggests that the model is realistically simulating the hydrodynamics and the parameters of the plasma. Moreover,

realization of the suggested experimental set-up will provide a precise knowledge for constructing much more complex experimental set-ups and other complex experiments that require more optics.

The main future goal of this work is to obtain a soft x-ray lasing but Nd:YAG laser specifications are not adequate solely, so we only modified the Mo preplasma condition which is a gain medium for the x-ray lasing which can be realized by using only several hundred mJ energy and only picoseconds pulse durations. When we use the CPA laser, which is under construction at the METU Laser Laboratory, as a main laser pulse for pumping the Mo preplasma, we can obtain x-ray lasing at 18.9 nm for Ni-like Mo resonance line spectrum and associated continuum emission with particular emphasis on the temporal behavior of the lasing and emission. The major goal which is much more important than the future goal is to use x-ray lasers as a source to x-ray laser holography, interferometry, radiography, and microscopy.

REFERENCES

- [1] Abou-Ali Y., Demir A., Tallents G. J., *et al.*, 2003, J. Phys. B: At. Mol. Opt. Phys., 36, 4097–4106
- [2] Abou-Ali Y., Dong Q.L., Demir A. *et al.*, 2004, J. Phys. B: At. Mol. Opt. Phys., 37, 2855–2868
- [3] Cairns G. F., Healyz S.B., Lewisy C. L. S. *et al.*, 1996, J. Phys. B: At. Mol. Opt. Phys., 29, 4839-4854
- [4] Chen F.F., 1984, Introduction to Plasma Physics and Controlled Fusion, Plenum Press, New York
- [5] Cooper J., 1966, Rep. Prog. Phys., **29**, 35-130
- [6] Daido H., 2002, Rep. Prog. Phys., 65, 1513–1576
- [7] De Michelis C., Mattioli M., 1984, Rep. Prog. Phys., 47, 1233-1346
- [8] Demir A., Phd Thesis, May 1997, “*Spectroscopy of X-Ray Laser Media*”, University of Essex
- [9] Demir A., Zeitoun P., Tallents G. J., *et al.*, 1997, Phys. Rev. E, 55/2, 1827-1835
- [10] Dendy R., 1993, Plasma Physics, Cambridge University Press
- [11] Eliezer S., Krumbein A.D., Salzmann D., 1978, J. Phys. D: Appl. Phys., 11, 1693-1701

- [12] Healy S. B., Cairns G. F., Lewis C. L. S., *et al.*, 1995, IEEE Journ.of Sel. Top.in Quant. Elect., 1/3, 949-957
- [13] Holden P. B., Healy B., Lightbody M.T.M., *et al.*, 1994, J. Phys. B: At. Mol. Opt Phys., 27, 341367
- [14] Kaçar E., Phd Thesis, Oct. 2004, “*Atom Numarası 18 ile 40 Arasında Olan Elementlerin Ne-Benzeri ve F-Benzeri İyonlarından Yayılan Spektrumların Hesaplanması*”, University of Kocaeli
- [15] Kawachi T., Kado M., Tanaka M., *et al.*, 2002, Phys. Rev. A, 66, 033815
- [16] Keenan R., Dunn J., Patel P. K., *et al.*, 2005, Phys. Rev. Let., PRL 94, 103901
- [17] Kenar N., Phd Thesis, November, 2004, “*Lazer Plazma Ortamlarından Yayılan X-Isını Rezonans çizgilerinin Modellenmesi ve Uygulama Alanlarının Belirlenmesi*”, University of Kocaeli
- [18] King R., Pert G.J., Aggarwal K. M., Keenan F. P., Rose S.J., 2004, J. Phys. B: At. Mol. Opt. Phys., 37, 225–236
- [19] Kuba J., Phd Thesis, Oct. 2001, “*Experimental and Theoretical Study of X-ray Lasers Pumped by an Ultra-Short Laser Pulse: Transient Pumping of Ni-like Ag Ions*” Czech Technical University
- [20] Larotonda M. A., Luther B. M., Wang Y., *et al.*, 2004, IEEE Journ.of Sel. Top.in Quant. Elect.,10/6, 1363-1367
- [21] Lee T. N., McLean E.A., Elton R. C., 1987, Phys. Rev. Let., 59/11, 1185-1188

- [22] Li R., Ozaki T., Kanai T., Kuroda H., 1998, *Phys. Rev. E*, 57/6, 7093-7102
Ozaki T., Ganeev R. A., Ishizawa A., *et al.*, 2002, *Phys. Rev. Let.*, 89/25, 253902
- [23] London R. A., Rosen M.D., Maxoni M.S., 1989, *J. Phys. B: At. Mol. Opt. Phys.*, 22, 3363-3376
- [24] Luca U. Labate, Phd Thesis, 2004, “*Progress in Laser-Plasma X-ray Sources: Time-Resolved Spectroscopic Studies and Applications to μ -imaging*” University of Bologna
- [25] MacGowan B. J., Maxon S., Da Silva L. B., *et al.*, 1990, *Phys. Rev. Let.*, 65/4, 420-423
- [26] Man B. Y., Dong Q. L., Liu A. H., *et al.*, 2004, *J. Opt. A: Pure Appl. Opt.*, 6, 17–21
- [27] Matthews D. L., Halgelstein P. L., Rosen M. D., *et al.*, 1985, *Phys. Rev. Let.*, 54/2, 110-114
- [28] McCabe S., Pert G.J., 2000, *Phys. Rev. A*, 61, 033804
- [29] Nickles P. V., Shlyaptsev V. N. , Kalachnikov M., *et al.*, 1997, *Phys. Rev. Let.*, 78/14, 2748-2751
- [30] Nilsen J., Macgowan B.J., Da Silva L.B., Moreno J. C., 1993, *Phys. Rev. A*, 48/6, 4682-4685
- [31] Nilsen J., Li Y., Dunn J., *et al.*, June 19-23, 2000, 7th International Conference on X-ray Lasers, Saint-Male, France

- [32] Ozaki T., Ganeev R. A., Ishizawa A., *et al.*, 2002, Phys. Rev. Let., 89/25, 253902
- [33] Pert G.J., 1983, J. Fluid Mech., 131, 401
- [34] Rocca J. J., 1999, Rev. of Scien. Ins., 70/10, 3799-3827
- [35] Smith R., Tallents G. J., Zhang J., Eker G., *et al.*, 1999, Phys. Rev. A, 59/1, R47-R50
- [36] Tallents G. J., 2003, J. Phys. D: Appl. Phys. 36, R259–R276
- [37] The Department of Physics, University of York, Heslington, York,
http://www.york.ac.uk/depts/phys/research/tallents/application_of_soft_x_ray_lasers.pdf, August 2006
- [38] Tommasini R., Nilsen J., Fill E. E., July 29-August 3, 2001, International Symposium on Optical Science and Technology San Diego, CA
- [39] Tümmler J., Janulewicz K. A., Priebe G. , Nickles P. V., 2005, Phys. Rev. E, 72, 037401

APPENDIX A: SPECIFICATIONS FOR TURBO PUMP

Table 4: Specifications for turbo pump Varian 551 TV navigator

CHARACTERISTIC	TV 551		TV 701
Pumping speed (with inlet screen) N ₂ : He: H ₂ :	CFF 6"/ ISO100: 350 l/s 450 l/s 450 l/s	CFF 8"/ ISO160: 550 l/s 600 l/s 510 l/s	CFF 10"/ ISO200: 690 l/s 620 l/s 510 l/s
Compression ratio N ₂ : He: H ₂ :	1 x 10 ⁹ 1 x 10 ⁷ 1 x 10 ⁸		1 x 10 ⁹ 1 x 10 ⁷ 1 x 10 ⁸
Base pressure <i>(According to standard DIN 28 428, the base pressure is that measured in a leak-free test dome, 48 hours after the completion of test dome bake-out, with a Turbopump fitted with a ConFlat flange and using the recommended pre-vacuum pump)</i>	with minimum recommended mechanical pump: < 1 x 10 ⁻¹⁰ mbar (< 1 x 10 ⁻¹⁰ Torr) with minimum recommended diaphragm pump: 2 x 10 ⁻⁹ mbar (1.5 x 10 ⁻⁹ torr)		
Inlet flange	ISO 160, ISO 100, CF 6", CF 8"		ISO 200, CF 10"
Foreline flange	KF 25 NW		
Rotational speed	42000 rpm		
Start-up time	< 5 minutes		
Recommended forepump Mechanical Dry	Varian DS 302 Varian Triscroll PTS 300		
Operating position	Any		
Operating ambient temperature	+5 °C to +35 °C		
Cooling requirements	Natural air convection Water optional (use water with electrical conductivity ≤ 500 μS/cm)		
Cooling water	flow: 200 l/h (0.89 GPM) temperature: + 10° C to + 30° C pressure: 3 to 5 bar (45 to 75 Psi)		
Bakeout temperature	120° C at inlet flange max. (CF flange) 80° C at inlet flange max. (ISO flange)		
Max permissible rotor temperature	120 °C		

Table 4: Continued

Vibration level (displacement)	< 0.01 μm at inlet flange	
Lubricant	permanent lubrication	
Noise level	<45 dB(A) at 1 meter	
Power supply: Input voltage: Input freq.: Max input power: Stand-by power: Max operating power:	100 to 240 Vac 50/60 Hz 600 VA 30 to 35 W TV 551: 325 W with water cooling 220 W with air cooling TV 701: 350 W with water cooling 250 W with air cooling	
Protection fuse	1 x 6.3 A	
Compliance with:	UNI EN 292-1 UNI EN 292-2 EN-CENELEC 55011 IEC 1000-4-2 (ex 801-2) IEC 1000-4-3 (ex 801-3) IEC 1000-4-4 (ex 801-4) EN 61010-1 (IEC 1010-1) EN 1012-2	
Power cable	With European or NEMA plug 3 meters long (optional)	
Serial communication (Navigator kit)	RS232 cable with a 9-pin D type male connector and a 9-pin D type female connector, and Navigator software (optional)	
Installation category	II	
Pollution degree	2	
Storage temperature	-20° C to +70° C	
Weight kg (lbs)		
ISO flange	19.4 (43)	19.4 (43)
CF flange	23.4 (51.6)	25.5 (54.2)
Controller	5.4 (12)	

APPENDIX B: SPECIFICATIONS FOR PULSED LASER

Table 5: Specifications for CFR400 Pulsed Nd:YAG Laser

	Wavelength (nm)	CFR400 Stable			CFR400GRM	
Repetition Frequency (Hz)		10	20	30	10	30
Pulse Energy (mJ)	1064	400	400	330	330	330
	532	230	230	190	190	170
	355				60	45
	355HE	90	90	80		
	266				40	30
1574	70	65	65			
Pulse Duration (ns) [1]		7-10			6 - 9	
Beam Divergence (mrad) [2]	1064	<4.5	<4.5	<5	<1.5	<1.5
	532	<3.5	<3.5	<4.5	<1.5	<1.5
	355				<1	<1
	355HE	<3.5	<3.5	<4		
	266				<1.2	<1.2
1574	<12	<12	<12			
Energy Stability (%) [3]	1064	<2	<2	<2	<2	<2
	532	<2.5	<2.5	<2.5	<2.5	<2.5
	355				<3	<3
	355HE	<2	<2	<2		
	266				<3	<3
1574	<5	<5	<5			
Beam Diameter (mm) [4]	All	7			7	
Pointing Stability (microrad) [5]	All	100			100	
Jitter, (+/-ns WRT Q-switch) [6]	All	<1			<1	
Specifications applying to all systems	Energy Drift over 8 Hours	<10%				
	Flashlamp Lifetime	>20 million Shots				
	Operating Temperature	10 - 40°C				
	Storage Temperature	5 - 50°C				
Ethylene Glycol Option [7]	Operating Temperature	-10 - 50°C				
	Storage Temperature	-30 - 70°C				

[1] Nominal FWHM

[2] Angle Containing 86.5% Energy. Other Methods can Predict Lower Values for GRM Systems

[3] Variation from Mean for 99% of Shots

[4] Nominal Value

[5] Full Angle, 99% of Shots

[6] Measured from Q-Switch Sync. Output

[7] 10% Energy Drop

APPENDIX C: SPECIFICATIONS FOR CCD CAMERA

Table 6: Specifications for Andor XUV CCD camera

Active Pixels (horiz x vert)	1024 x 256 Pixel
Pixel Size (horiz x vert; μm)	26 x 26
Image Area (horiz x vert; mm)	26.7 x 6.7
Sensor option	FI, FI-DD, BV, BN, FO, FB
Frame Rate/ 4×4 binned frame rate (frames/sec)	3.3/10.3
Spectral rate (spectra per second)	166 (500)
Pixel readout rate	1 MHz, 0.5 MHz, 66 kHz, 31 kHz
Read Noise (e^-)	4
Digitization	16-bit
Software Selectable Pre-Amplifier Sensitivity	Yes